8-7-2012

Magnetotransport in Two Dimensional Electron Systems Under Microwave Excitation and in Highly Oriented Pyrolytic Graphite

Aruna N. Ramanayaka
Georgia State University

Recommended Citation

Ramanayaka, Aruna N., "Magnetotransport in Two Dimensional Electron Systems Under Microwave Excitation and in Highly Oriented Pyrolytic Graphite." Dissertation, Georgia State University, 2012.
https://scholarworks.gsu.edu/phy_astr_diss/54

MAGNETOTRANSPORT IN TWO DIMENSIONAL ELECTRON SYSTEMS UNDER MICROWAVE EXCITATION AND IN HIGHLY ORIENTED PYROLYTIC GRAPHITE

by

ARUNA N. RAMANAYAKA

Under the Direction of Dr. Ramesh G. Mani

ABSTRACT

This thesis consists of two parts. The first part considers the effect of microwave radiation on magnetotransport in high quality GaAs/AlGaAs heterostructure two dimensional electron systems. The effect of microwave (MW) radiation on electron temperature was studied by investigating the amplitude of the Shubnikov de Haas (SdH) oscillations in a regime where the cyclotron frequency ω_c and the MW angular frequency ω satisfy $2\omega \leq \omega_c \leq 3.5\omega$. The results indicate negligible electron heating under modest MW photoexcitation, in agreement with theoretical predictions. Next, the effect of the polarization direction of the linearly polarized MWs on the MW induced magnetoresistance oscillation amplitude was investigated. The results demonstrate the first indications of polarization dependence of MW induced magnetoresistance oscillations. In the second part, experiments on the magnetotransport of three dimensional highly oriented pyrolytic graphite (HOPG) reveal a non-zero Berry phase for HOPG. Furthermore, a novel phase relation between oscillatory magneto- and Hall- resistances was discovered from the studies of the HOPG specimen.

INDEX WORDS: Two dimensional electron systems, Magnetoresistance, Microwave induced magnetoresistance oscillations, Graphite, Quantum Hall effect, Hall effect, Resistivity rule, Shubnikov de Haas effect, Shubnikov de Haas oscillations

MAGNETOTRANSPORT IN TWO DIMENSIONAL ELECTRON SYSTEMS UNDER MICROWAVE EXCITATION AND IN HIGHLY ORIENTED PYROLYTIC GRAPHITE

by

ARUNA N. RAMANAYAKA

A Dissertation Submitted in Partial Fulfillment of the Requirements for the Degree of

Doctor of Philosophy
in the College of Arts and Sciences
Georgia State University
2012

MAGNETOTRANSPORT IN TWO DIMENSIONAL ELECTRON SYSTEMS UNDER MICROWAVE EXCITATION AND IN HIGHLY ORIENTED PYROLYTIC GRAPHITE

by

ARUNA N. RAMANAYAKA

Committee Chair: Dr. Ramesh G. Mani

Committee: Dr. A. G. Unil Perera
Dr. Vadym Apalkov
Dr. Murad Sarsour
Dr. Douglas Gies

Electronic Version Approved:

Office of Graduate Studies
College of Arts and Sciences
Georgia State University
August 2012

To my wife Sajini, parents and family

ACKNOWLEDGEMENTS

I am truly grateful to my thesis advisor, Professor Ramesh G. Mani, for his continuous guidance and support, and for providing an inspiring atmosphere for research. Also I would like to thank past and present members of the Nanoscience, Low Temperature and High Magnetic Field Laboratory for their support and encouragement. Further I would like to thank my thesis committee members for their support and guidance. I would like to acknowledge Georgia State University for providing financial support and research opportunities, and also the funding agencies Army Research Office (ARO) and Department of Energy (DOE) for the financial support of the research. Last, but not least, I would like to thank my wife Sajini, my family, teachers, and my friends who helped me to become the person who I am.

TABLE OF CONTENTS

LIST OF TABLES

LIST OF FIGURES

LIST OF ABBREVIATIONS

- 2DEG - Two Dimensional Electron Gas
- 2DES - Two Dimensional Electron System
- ABR - Allen Bradley Resistor
- ARPES - Angle Resolved Photo Emission Spectroscopy
- AWG - American Wire Gauge
- dHvA - de Haas -van Alphen
- FQHE - Fractional Quantum Hall Effect
- HOPG - Highly Oriented Pyrolytic Graphite
- IQHE - Integer Quantum Hall Effect
- LLCC - Leadless Chip Carrier
- MW - Microwave
- MIMO - Microwave Induced Magnetoresistance Oscillations
- MIRO - Microwave Induced Resistance Oscillations
- NLSF - Nonlinear Least Square Fit
- SdH - Shubnikov de Haas
- TTL - Transistor Transistor Logic
- UHV - Ultra High Vacuum
- VTI - Variable Temperature Inset

- w/ - with
- w/o - without
- i.d. - inner diameter
- o.d. - outer diameter
- ZRS - Zero Resistance State

CHAPTER 1

INTRODUCTION

The dissertation consists of two parts. The first part is based on two key aspects of electrical transport in two-dimensional electron systems (2DES) under microwave irradiation, namely the possibility of heating effects under microwave irradiation and polarization sensitivity of microwave induced magnetoresistance oscillations. The second part of the dissertation is focused on electrical transport in low-dimensional, highly oriented pyrolytic graphite (HOPG) at low temperature and at high magnetic fields motivated by the remarkable electronic properties observed in graphene. Chapter 2 reviews the basic physical concepts of 2DES including a brief introduction to GaAs/AlGaAs heterostructures, section 2.2, behaviour of a 2DES in a magnetic field, section 2.3, Drude model of electrical conductivity, section 2.4, integer quantum Hall effect (IQHE), section 2.5, fractional quantum Hall effect (FQHE), section 2.6, etc.

In Chapter 3, I summarize the experimental and theoretical work that has been done in the field of microwave induced electrical transport in 2DES since the discovery of zero resistance states (ZRS) of the microwave induced magnetoresistance oscillations (MIMO).[11] After a brief introduction to the previous work on MIMO, I describe the experimental work done during this study.

In Chapter 4, I discuss about the influence of microwave photoexcitation on the amplitude of SdH oscillations in a GaAs/AlGaAs 2DES in a regime where strong MIMO can be observed. A SdH lineshape analysis indicates that increasing the incident microwave power has only a weak affect on the amplitude of the SdH oscillations, in comparison to the influence of modest temperature changes on the dark-specimen SdH effect. The results indicate negligible electron heating under modest microwave photoexcitation, in good agreement with theoretical predictions. This work has already been published in ref. [39].

Next, Chapter 5 describes the experimental work on the polarization sensitivity of MIMO by rotating, by an angle θ, the polarization of linearly polarized microwaves with respect to the long-axis of GaAs/AlGaAs Hall-bar electron devices. At low microwave power P, experiments show a strong sinusoidal variation in the diagonal resistance R_{xx} vs θ at the oscillatory extrema, indicating a linear polarization sensitivity in the microwave radiation-induced magnetoresistance oscillations. Surprisingly, the phase shift θ_0 extracted from lineshape fits of maximal oscillatory R_{xx} response under photoexcitation appears dependent upon the radiation-frequency f, the magnetic field B, and the magnetic field orientation, i.e., sign of (B). To date, these results illustrate the first experimental observations of the polarization sensitivity of MIMO, and this work has been published in ref. [70] and ref. [71].

I present in Chapter 6 the experimental studies on electrical transport in three-dimensional HOPG. Transport measurements indicate strong oscillations in the Hall-, R_{xy}, and the diagonal-, R_{xx}, resistances, and the measurements exhibit Hall plateaus at the lowest temperatures. At the same time, a comparative analysis of the SdH oscillations and Berry's phase indicates that graphite is unlike the GaAs/AlGaAs 2DES, the 3D n-GaAs epilayer, semiconducting $Hg_{0.8}Cd_{0.2}Te$, and some other systems. Further, we observe the transport data to follow $B \times dR_{xy}/dB \approx -\Delta R_{xx}$, and this feature is consistent with the observed anomalous relative phases of the oscillatory R_{xx} and R_{xy}. This work has been published in ref. [111].

The last chapter, Chapter 7, summarize the results reported in the dissertation and discuss the possibilities of other experiments can be carried out in the future using the experimental setup developed during this work.

Appendix A provides a detailed description of the experimental apparatus used for the experiments reported in this dissertation. A detailed description of the sample holder (or probe) and its design is given in Appendix A.1. In the second part, a detailed description of the design of the microwave launcher and its working principal is given (Appendix A.1.1). In the third part (Appendix A.1.2), the design of the sample mount, which enabled us to connect several different types of sample carriers to the sample probe, is described. Finally, the experimental details of the temperature measurements and control are given in Appendix A.2.

A brief description of the electrical measurements carried out using low frequency lock-in technique is given in Appendix B. Finally, Appendix C provide a brief description for the procedures used for preparing Hall bar devices from high quality GaAs/AlGaAs heterostructures and thin HOPG specimen starting from bulk HOPG.

CHAPTER 2

TWO DIMENSIONAL ELECTRON SYSTEMS

2.1 Introduction

Beside the remarkable discoveries such as superconductivity (H. K. Onnes, 1911), superfluidity in helium-4 (P. Kapitsa, 1938), the transistor (W. Shockley, J. Bardeen, and W. Brattain, 1947), and superfluidity in helium-3 (D. M. Lee, D. D. Osheroff, and R. C. Richardson, 1972), most of the other discoveries in condensed matter physics have come from the studies of reduced dimensional systems, especially 2D. These amazing properties become visible in reduced dimensions due to the fact that the carriers are confined in a region with the dimensions comparable to the de Broglie wavelength. Let us consider a situation where the carriers are confined in an infinitely deep potential well of width a. From the basic quantum mechanics, we know that the energy of the carriers is quantized and can be written as

$$E_M = \frac{\pi^2 \hbar^2 M^2}{2m^* a^2} \tag{2.1}$$

where m^* is the effective mass of the carriers and $M = 1, 2, ...$ is the quantum number of a given energy state. In fact, size quantized structures do not have a infinite potential well. Yet for a potential well with a finite depth the quantized energy level can, approximately, be written as [1]

$$E_M \sim \frac{\hbar^2}{m^* a^2}. \tag{2.2}$$

If the carriers are only confined in one z-direction, they they are free to move in xy-plane. In such a situation the total energy of a size quantized system is given by

$$E = E_M + \frac{p_x^2 + p_y^2}{2m^*} \tag{2.3}$$

where p_x, and p_y are momentum components in the respective directions. Confining the carriers in a well is not enough to observe size quantization effects. There are other conditions that have to satisfy in order to achieve an observable effect due to size quantization.

A sufficiently large energy level separation is required for an observable energy quantization due to quantum size effects. In addition, the separation of two neighboring energy levels must be greater than the thermal energy of the carriers,

$$E_{M+1} - E_M \gg kT. \tag{2.4}$$

It is important to note that these energy levels, E_M, are due to size quantization only, and not due to an applied magnetic field. If the electron gas is degenerate, then following condition is also desirable,

$$E_2 > E_F > E_1 \tag{2.5}$$

where E_1 and E_2 are the energies of the first and second energy levels, in order to have an observable effect due to size quantization.[1]

In real systems, carriers always undergo scattering due to phonons, impurities, defects, etc. For a given system, the scattering probability is characterized by the single particle lifetime τ_s, where the value of τ_s represents the average lifetime of carriers in a quantum state. The Heisenberg uncertainty principal requires that $\Delta t \Delta E \sim \hbar$. Consequently, a finite value of τ_s results in an uncertainty in the energy of a given quantum state, i.e., $\Delta E \sim \hbar/\tau_s$. In this situation, the energy separation of the quantized energy levels must be greater than ΔE:

$$E_{M+1} - E_M \gg \frac{\hbar}{\tau_s}. \tag{2.6}$$

Furthermore, transport lifetime τ is proportional to the carrier mobility $\mu = e\tau/m^*$. Thus, the observation of quantum size effects demands that the system must have properties such as small layer thickness, high carrier mobilities, lower temperatures, high surface quality, and not very high carrier concentrations.

Over the past few decades, scientists have been using different material systems, such as semimetallic Bi thin films, Silicon MOS structures, and heterostructures, etc., to study these quantized size effects. After enormous progress in the field, quantum heterostructures appear to be the best material known for studying quantum size effects, in particular, MBE grown GaAs/AlGaAs heterostructures.

2.2 GaAs/AlGaAs heterostructures

A heterojunction is formed by contacting two materials with different band gaps. Atomically smooth interfaces and low density of states can be achieved in a heterostructure by choosing the semiconductors with proper lattice match. Heterostructures, therefore, can provide extremely high quality devices in comparison with Silicon MOS structures or semimetalic thin films.

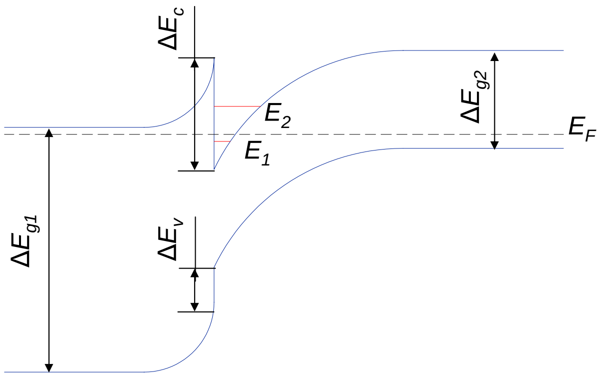

Figure 2.1 A typical band diagram of a heterojunction between n-type and p-type semiconductors. Here $\Delta E_v = E_{g1} - E_{g2} - \Delta E_c$, where ΔE_c is the difference between the electron affinities of the two materials, i.e., $\Delta E_c = \chi_2 - \chi_1$.[1]

Figure 2.1 illustrates a typical energy band diagram of a single heterojunction between n-type and p-type semiconductors. Here E_{g1}, and E_{g2} are the band gaps of the two materials and $\Delta E_v = E_{g1} - E_{g1} - E_c$, where $\Delta E_c = \chi_2 - \chi_1$, χ_1, χ_2 are the electron affinities of materials 1 and 2, respectively. As in all the other systems, 2DES formed in heterojunctions also suffer the problem of scattering. There are several types of scatters in heterostructures, such as ionized impurities, phonons, interface roughness, etc.

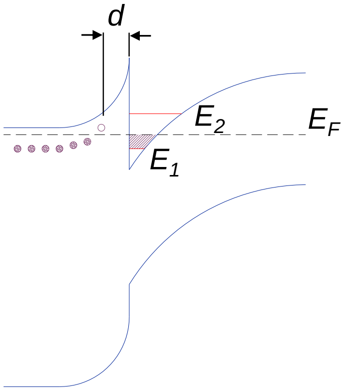

Figure 2.2 Energy band diagram of a modulation doped heterojunction.[1]

Interface scattering can be controlled to extremely low levels in heterojunctions due to extremely smooth interface between two semiconductors, e.g. GaAs/AlGaAs heterojunctions, compared that of MOS-structures. Acoustic phonon and impurity scattering has T^{-1} and $T^{3/2}$ dependence on carrier mobility μ in 2DES, respectively, where in bulk semiconductors $\mu \sim T^{-3/2}$ for acoustic phonon scattering and $\mu \sim T^2$ for impurity scattering.[1] Hence phonon scattering can be suppressed at cryogenic temperatures. Yet the scattering due to ionized impurities remain. In order to reduce the ionized impurity scattering one can decrease the doping level but this method would not work as the reduction in doping reduces the electron concentration. Modulation doping has been proposed [8, 9] to overcome this problem. Energy band diagram of a modulation doped heterojunction is shown in Figure 2.2. In a typical modulation doped heterojunction, the narrow gap material is undoped and the wide gap material is doped. Some carriers pass into the narrow gap semiconductor forming a layer of electrons near the interface (Figure 2.2) to equalize the chemical potential in both semiconductors. Now the electron layer is in the narrow gap side of the junction and the ionized impurities are in the other (wide gap) side; therefore, the separation of ionized impurities and the layer of electrons at the interface results in increasing the mobility of the carriers. Furthermore, one can increase the width of the undoped region d (Figure 2.2) in order to further separate the ionized impurities and the electron layer, and this would indeed increase the mobility. But the mobility will increase with d only up to a certain limit, and after that it will cause a decrease in carrier concentration.

Modulation doped heterojunctions can readily provide a potential well for both types of charge carriers at the inversion layer (Figure 2.2) depending on the doping, i.e., p-type or n-type, with extremely high carrier mobility. It is important to note that the expression for size quantized energy levels E_M in eq. (2.1) is no longer accurate for heterojunction structures as these do not provide a perfect straight wall potential well; therefore, a more detailed analysis will be needed to evaluate E_M for these heterojunction structures.

2.3 2DES in a magnetic field

In principal externally applied magnetic field can be divided into two components when considering a 2DES, namely in plane and out of plane. It can be shown that the in plane magnetic field component does not change the energy spectrum qualitatively [1], yet it change both the energy of the size quantization and the effective mass for motion normal to the direction of the applied magnetic field.[1] The out of plane component, however, will change the energy spectrum significantly.

Let us consider a situation where the applied magnetic field is perpendicular to the 2D plane and there is no in plane field component for the simplicity of the derivation. In this situation, the applied magnetic field does not influence the electron motion along the z-axis, and hence there is no change in the size quantized energy level, which is still controlled by the quantum well potential. Motion of spin-less, non-interacting, massive electrons in xy-plane can be written as

$$-\frac{\hbar^2}{2m^*}\left[\left(-i\frac{\partial}{\partial x}-\frac{eB}{\hbar}\right)^2-\frac{\partial^2}{\partial y^2}\right]\cdot\psi(x,y)=E_\perp\cdot\psi(x,y) \tag{2.7}$$

for a vector potential

$$A_x=-yB, A_y=0 \tag{2.8}$$

where B is the magnetic field applied in the z direction. Let us assume a wave function of the form

$$\psi(x,y) = e^{ip_x x/\hbar}\chi(y). \tag{2.9}$$

By substituting eq. (2.9) in eq. (2.7), we get a harmonic oscillator equation

$$-\frac{\hbar^2}{2m^*}\chi'' + \frac{m^*\omega_c^2(y-y_0)^2}{2}\chi = E_\perp\chi \tag{2.10}$$

with the oscillator center position y_0, where

$$y_0 = -\left(\frac{1}{eB}\right)p_x \tag{2.11}$$

for

$$l_0 = \sqrt{\hbar/eB} \tag{2.12}$$

where l_0 is the magnetic length or the characteristic size of an electron orbit. Substituting from eq. (2.12) in eq. (2.11), for the ground state of a Landau oscillator, y_0 can be written as

$$y_0 = -l_0^2\left(\frac{p_x}{\hbar}\right) \tag{2.13}$$

and ω_c is the cyclotron frequency.

$$\omega_c = \frac{eB}{m^*}. \tag{2.14}$$

Then the total energy can be written as

$$E = E_M + \hbar\omega_c(N + 1/2) \tag{2.15}$$

where $N = 0, 1, 2, ...$ for $\hbar\omega_c(n+1/2)$ are the energy eigenvalues $E_\perp$ of eq. (2.10) also known as the Landau levels (LL).

Taking into account electron spin, each LL is split into two energy levels separated by Zeeman energy

$$E = E_M + \hbar\omega_c(N + 1/2) \mp \frac{1}{2}\mu_B g B \tag{2.16}$$

where g is the electron g-factor and μ_B is the Bohr magneton, and the minus ($-$) and plus ($+$) signs corresponds to the spin up ($\uparrow$) and down ($\downarrow$) states of the electrons, respectively. Therefore, in an ideal 2DES subjected to a magnetic field B normal to the 2D plane, the energy spectrum consists of size quantized energy levels, and Landau levels separated by cyclotron gaps $\hbar\omega_c$ which are further spin-split by Zeeman energy $\mu_B gB$. Remarkably, in this situation the energy spectrum of the carriers is discrete.

Typically the energy separation in size quantized energy levels is considerably greater than the Fermi energy E_F at low temperatures,

$$E_F = \frac{\hbar^2 k_F^2}{2m^*}. \tag{2.17}$$

Therefore, the lowest sub-band of the size quantized energy levels is occupied and the eq. (2.16) becomes

$$E = E_1 + \hbar\omega_c(N + 1/2) \mp \frac{1}{2}\mu_B gB \tag{2.18}$$

where E_1 is the lowest sub-band of the size quantized energy levels.

Motion in the 2D plane (xy-plane) under a non-zero magnetic field applied in the z direction is described by the momentum component p_x and the discrete LL index N. The energy depends only on N and the spin direction, so the Landau levels are degenerate over the momentum p_x or the oscillator position y_0 [eq. (2.11)]. It can be shown that the LL degeneracy is $L_x L_y \times 1/2\pi l_0^2$, where L_x and L_y are the sample dimensions in x- and y- directions, respectively. Consequently, LL degeneracy per unit area can be written as $(2\pi l_0^2)^{-1}$ since $L_x L_y$ is the sample area. Hence the density of states for a given LL can be written as

$$n_{DS} = \frac{eB}{h} \tag{2.19}$$

for $l_0 = \sqrt{\hbar/eB}$ [eq. (2.12)]. When electrons are put into these states, the number of Landau levels filled is defined as the filling factor ν,

$$\nu = \frac{n}{n_{DS}} \tag{2.20}$$

where n is the density of the charge carriers. This indicates that the filling factor $\nu \propto B^{-1}$, from eq. (2.19) and eq. (2.20). The density of states given in eq. (2.19) represents the density of states per LL; therefore, one would have to multiply eq. (2.19) by the corresponding degeneracy factor to find the density of states for a degenerate electron system.

2.4 Electrical conductivity - Drude model

Let us now consider the electrical conduction in system based on the Drude model, which is constructed in the early 1900s by P. Drude to describe the electrical conduction in metals.[2] The Drude model for electrical conduction is based on the kinetic theory of gases and the following assumptions. First, the independent electron approximation: there are no electron-electron interactions between collisions. Next, the free electron approximation: there are no electron-ion interactions. Hence, in the absence of an externally applied electric or magnetic field, electrons will have a uniform straight line motion. Second, the collisions between electron and ions are instantaneous, uncorrelated events that will only result in an abrupt change in the electron velocity. Third, the probability of an electron having a collision in a time interval dt is dt/τ, where τ is independent of the electron position or momentum. Fourth, only the collisions are responsible for the electrons achieving thermal equilibrium with their surroundings.

The resistivity ρ can be defined as the proportionality constant between the electric field E and the current density j.

$$E = \rho j. \tag{2.21}$$

Then the current density j can be defined as

$$j = -nev_{avg} \tag{2.22}$$

where n, v_{avg} are the number of electrons per unit volume and the average electron velocity, respectively. The average velocity can be written as

$$v_{avg} = -\frac{eE\tau}{m} \tag{2.23}$$

where the minus $('-')$ sign is due to the movement of the electrons in a direction opposite to the applied electric field. Then from eq. (2.22) and eq. (2.23)

$$j = \sigma_0 E \tag{2.24}$$

where σ_0 is the conductivity and is given by

$$\sigma_0 = \frac{ne^2\tau}{m}. \tag{2.25}$$

2.4.1 Electronic transport in an electric and a magnetic field

Let us consider the classical motion of an electron in the presence of an electric and a magnetic field.

$$m\dot{\overrightarrow{v}} + \frac{m\overrightarrow{v}}{\tau} = -e\left(\overrightarrow{E} + \overrightarrow{v} \times \overrightarrow{B}\right) \tag{2.26}$$

Here, $m\overrightarrow{v}/\tau$ accounts for electron scattering due to disorder, and for the purpose of this discussion, let us consider $\overrightarrow{E} = E\widehat{x}$ and $\overrightarrow{B} = B\widehat{z}$. Now for the steady state, from eq. (2.26),

$$\frac{m\overrightarrow{v}}{\tau} + e\left(\overrightarrow{E} + \overrightarrow{v} \times \overrightarrow{B}\right) = 0. \tag{2.27}$$

Let us consider the matrix form of eq. (2.27) in 3D,

$$\begin{pmatrix} \frac{m}{\tau} & eB & 0 \\ -eB & \frac{m}{\tau} & 0 \\ 0 & 0 & \frac{m}{\tau} \end{pmatrix} \begin{pmatrix} v_x \\ v_y \\ v_z \end{pmatrix} = -e \begin{pmatrix} E \\ 0 \\ 0 \end{pmatrix}. \tag{2.28}$$

Comparing eq. (2.23), eq. (2.25), and eq. (2.28), conductivity σ can be written as,

$$\sigma = ne^2 A^{-1} \tag{2.29}$$

where

$$A = \begin{pmatrix} \frac{m}{\tau} & eB & 0 \\ -eB & \frac{m}{\tau} & 0 \\ 0 & 0 & \frac{m}{\tau} \end{pmatrix}. \tag{2.30}$$

From eq. (2.25), eq. (2.29) and eq. (2.30), it can be shown that

$$\sigma = \frac{\sigma_0}{1+\omega_c^2\tau^2} \begin{pmatrix} 1 & -\omega_c\tau & 0 \\ \omega_c\tau & 1 & 0 \\ 0 & 0 & \frac{1}{1+\omega_c^2\tau^2} \end{pmatrix} \tag{2.31}$$

where ω_c is the cyclotron frequency, eq. (2.14). Here one can see that $\sigma_{zz} = \sigma_0$ since there is no force along the z direction due to the E or B field. Also the conductivity along the y direction has changed due to the applied magnetic field in the z direction, and is given by $\sigma_{xy} = -\sigma_{yx} = \omega_c\tau\sigma_0/(1+\omega_c^2\tau^2)$. The appearance of a voltage (Hall voltage) across a thin conducting film perpendicular to the current flow through the conducting film and a magnetic field, which is also perpendicular to the current, was discovered by E.H. Hall in 1879 and is known as the Hall effect. The minus sign in $\sigma_{xy} = -\sigma_{yx}$ represents the polarity of the Hall electric field, and the direction of the Hall electric field can be changed by reversing the magnetic field or the electric field.

2.5 Integer quantum Hall effect

About 100 years after the great discovery of the Hall effect by E. H. Hall in 1879, K. von Klitzing discovered the quantized Hall effect (see Figure 2.3), which later became known as the integer quantum Hall effect (IQHE). According to the first report of IQHE [5], Hall resistance at the plateau is independent of the geometry of the device and only dependent on the speed of light and the fine structure constant.

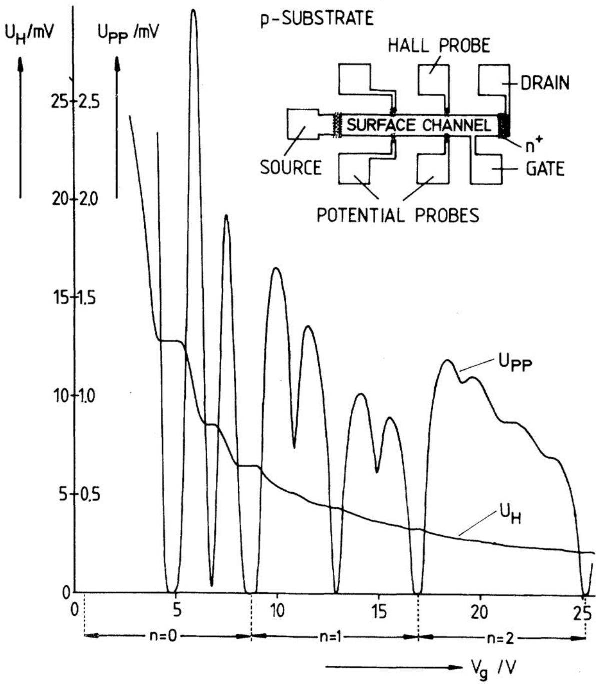

Figure 2.3 The first observation of the quantized Hall voltage. The voltage drop between the potential probes U_{pp} and the Hall voltage U_H vs the gate voltage V_g at $T = 1.5$ K. The constant magnetic field B is 18 Tesla and the source drain current, I, is 1 μA. The inset illustrates a top view of the device. After von Klitzing et al. (1980).[5]

In the first observation of the IQHE [5], the experiment has been carried out by measuring the longitudinal (U_{pp}) and transverse (U_H) voltages vs the gate voltage at a constant magnetic field (Figure 2.3). A high magnetic field, 18 Tesla, was used in ref. [5], and the Landau levels are well separated. The Fermi energy is a function of carrier concentration, and by changing the gate voltage one can change the charge carrier concentration in the system. Consequently, by changing the gate voltage one can move the Fermi energy relative to the Landau levels.

A similar scenario can be achieved by varying the magnetic field (Figure 2.4). In the absence of an external magnetic field, i.e., $B = 0$, the density of states have a constant value as function of energy [Figure 2.4 (a)]. Let us consider a situation where there is an applied magnetic field along the z-axis of the device. In an ideal situation, the Landau levels are

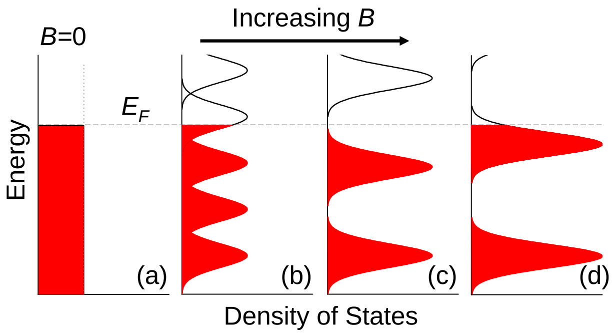

Figure 2.4 Landau level spectrum at different magnetic fields for a spin degenerate 2DES. (a) At $B = 0$ there is no separation of Landau levels; therefore, the density of states have a constant value vs the energy. (b) At a finite but small magnetic field, Landau levels are formed but not yet fully separated. Fermi energy E_F lies in the middle of a LL. (c) At this magnetic field the Landau levels are completely separated and E_F lies in between 2nd and 3rd Landau levels. In this situation the filling factor is equal 4, i.e., $\nu = 4$. (d) Magnetic field is at even higher value and E_F lies within a LL.

considered to be delta functions with zero width, yet under real experimental conditions due to scattering these delta function will be broadened; therefore, at smaller magnetic fields even the Landau levels are formed will not be separated from each other [Figure 2.4 (b)], i.e., the LL separation $\hbar\omega_c$ has to be greater than the width of the LL. As the magnetic field increases the separation between the Landau levels will increase; as a result, the overlap between two Landau levels would become smaller and smaller. In addition, as the magnetic field is swept the Landau levels move relative to the Fermi energy.

Let us consider a situation where the E_F lies in between two Landau levels and all the states below the Fermi level are occupied [Figure 2.4 (c)]. According to the Pauli exclusion principle, electrons inside these states are not allowed to scatter to other states. Consequently, all scattering events are suppressed and at this point the transport is dissipationless and the resistance goes to zero.

Classically, in strong magnetic fields $\omega_c\tau \gg 1$,

$$\sigma_{xx} = \frac{e^2 n}{m^* \omega_c^2 \tau} \tag{2.32}$$

$$\sigma_{xy} = \frac{e^2 n}{m^* \omega_c} \tag{2.33}$$

where σ_{xx} and σ_{xy} are the diagonal and Hall conductivities, respectively [see eq. (2.31)]. Let us assume that $B = B_N$ when E_F lies between N and $N+1$ Landau levels or between spin up ($\uparrow$) and spin down ($\downarrow$) levels of the Nth LL. Then from eq. (2.19) and eq. (2.33) we get

$$\sigma_{xy} = \left(\frac{e^2}{h}\right) \nu_N. \tag{2.34}$$

Remarkably during the same B-interval, where E_F lies in between two Landau levels, i.e., when the longitudinal resistance goes to zero (see Figure 2.3), Hall conductivity depends only on e, h, and ν_N. Further it is quantized at integer multiples of e^2/h.

2.5.1 Shubnikov de Haas oscillations

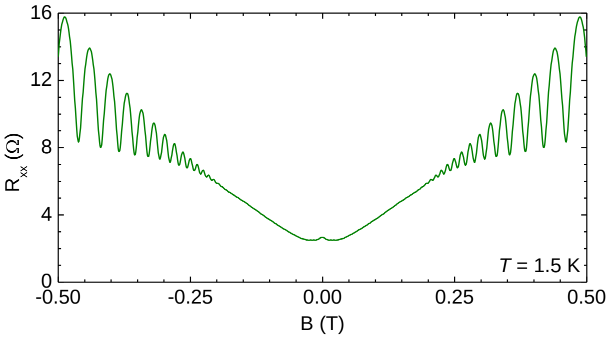

Figure 2.5 Shubnikov de Haas oscillations in a GaAs/AlGaAs Hall bar device at 1.5 K.

At high enough magnetic fields there exists energy gaps in the LL energy spectrum; consequently, the density of states becomes a discrete function of $1/B$, yet at lower magnetic fields, where the Landau levels are not completely separated from each other [Figure 2.4 (b)], the density of states becomes a continuous periodic function of $1/B$ and it reflects in longitudinal resistance as oscillations (Figure 2.5). These oscillations are called Shubnikov de Haas (SdH) oscillations. Furthermore, these oscillations are periodic in inverse magnetic field, i.e., $1/B$ (Figure 2.5) and F is the frequency of the SdH oscillations. The oscillatory part of the magnetoresistance ΔR_{xx}, i.e., only the SdH oscillations without the background, can be expressed in the following form [12]

$$\Delta R_{xx} = R_0 \frac{X_T}{\sinh(X_T)} \exp(-\pi/\omega_c \tau) \cos\left(2\pi \frac{E_F - E_M}{\hbar\omega_c} - \phi\right) \tag{2.35}$$

where R_0 is the zero field resistance, k_B is the Boltzmann constant, E_M is the energy of the Mth sub-band. The factor $X_T/\sinh(X_T)$ is the temperature dependence of the SdH oscillation amplitude and X_T is given by [36]

$$X_T = \frac{2\pi^2 k_B T}{\hbar\omega_c}. \tag{2.36}$$

Experimentally ΔR_{xx} is often considered as a exponentially damped cosine function [39]

$$\Delta R_{xx} = A e^{-\alpha/B} \cos(2\pi F/B) \tag{2.37}$$

where A is the amplitude of the oscillations, α is the damping factor, and F is the frequency. The frequency F of the SdH oscillations is a measure of the carrier density.

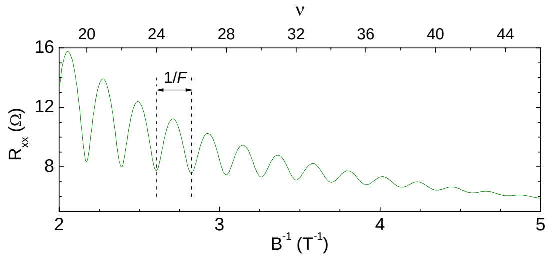

Figure 2.6 Periodicity of SdH oscillations vs $1/B$. Here F is the frequency of the SdH oscillations, and the corresponding filling factor ν is shown in the top axis.

The density n of the 2DES can be extracted from the frequency F of the SdH oscillations. In addition, the effective mass m^*, the mass that the electron experience while moving relative to the lattice in an applied electric or magnetic field, can be calculated from the temperature dependence of the SdH oscillation amplitude, and the scattering time τ can be extracted from the $1/B$ dependence of the SdH oscillation amplitude. Therefore, a study of SdH oscillations at low temperature and low magnetic fields will be beneficial for measuring the parameters, such as effective mass m^*, scattering time τ, and density n. As the oscillation amplitude depends on the temperature we can use it to probe possibility of heating effects in a 2DES due to radiation (see Chapter 4 for further details).

2.6 Fractional quantum Hall effect

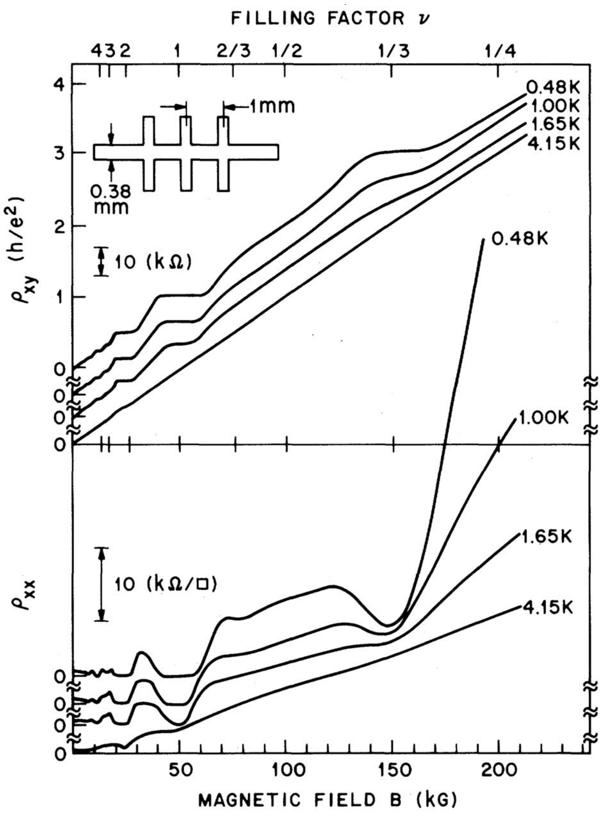

Figure 2.7 The first observation of the quantized Hall voltage at fractional filing factors $\nu = 1/3$. Magnetic field dependence of ρ_{xy} and ρ_{xx} is shown for a GaAs/$\mathrm{Al_{0.3}Ga_{0.7}}$As sample with $n = 1.23 \times 10^{11}$ cm^2, $\mu = 90 \times 10^3$ cm/V s, using $I = 1$ μA. The Landau level filling factor is defined by $\nu = nh/eB$. After Tsui et al. (1982).[6]

As we already discussed in section 2.5, as the applied external magnetic field increases the Landau levels go to higher and higher energies with respect to E_F (Figure 2.4). Let us consider situation where $v < 1$, which can be achieved in extremely high quality specimen at high enough magnetic fields and low temperatures. At higher magnetic fields l_0 becomes extremely small [eq. (2.12)]; consequently, it is important to consider the electron-electron interactions to understand the behaviour of the carriers in such a system.[4]

Few years after the discovery of IQHE, the experimental work by D. C. Tsui and H. L. Störmer led to the observation of a Hall plateau at a fractional filling factor $\nu = 1/3$ (see Figure 2.7) for the first time.[6] The fractional quantum Hall effect (FQHE) is characterized by the observation of vanishing R_{xx} and quantization of R_{xy} at fractional filling factors (see Figure 2.8). The FQHE state is an intrinsically many body, incompressible quantum liquid, is often described by the Laughlin wavefunction.[4, 7]

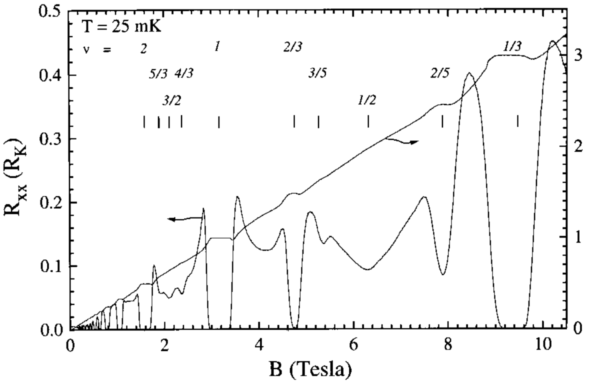

Figure 2.8 Longitudinal resistance, R_{xx}, and the transverse resistance, R_{xy}, measured in a GaAs/AlGaAs heterostructure device are plotted vs the magnetic field B. A series of Hall plateaus at fractional filling factors can be observed. After Mani et al. (1996).[10]

In a remarkable experimental observation, Mani et al. [10] describe a fractal nature of FQHE. According to the authors, it is possible to reconstruct the main sequence of FQHE for $\nu < 1$ using IQHE where filling factor $\nu > 1$. Furthermore, this reconstruction of the fractional quantum Hall states suggests a possibility of finding the missing fractions in the experimental observations.

CHAPTER 3

ELECTRICAL TRANSPORT IN 2DES UNDER MW IRRADIATION

In Chapter 2 we already discussed the interesting physical phenomenon that have been observed in 2DES, and most interestingly the vanishing resistance under IQHE[5], section 2.5, and FQHE[6, 7], section 2.6, conditions. In 2002 Mani et al. reported their experimental results[11] on discovering a zero resistance state in a 2DES under microwave irradiation at low temperatures. Major part of the thesis is based on these MW induced magnetoresistane oscillations (MIMO) observed in 2DES; therefore, this chapter will give a brief introduction to the to the MW induced ZRS and to MIMO.

3.1 Microwave induced zero resistance states

Figure 3.1 illustrates R_{xx} vs B response upto 10 Tesla for a high mobility 2DES specimen under microwave irradiation at $f = 103.5$ GHz. It can be easily seen the existence of Hall plateaus and zero resistance at higher magnetic fields, and also there is an extra set of resistance oscillations appear at the low magnetic fields under MW irradiation, see Figure 3.1 inset. A closer look at the behaviour of R_{xx} at low magnetic fields under MW irradiation reveals that the minima of these oscillations actually reach zero (Figure 3.2).

The behaviour of R_{xx} with and without MW radiation as a function of B is shown in Figure 3.2 for $f = 103.5$ GHz at low magnetic fields. It is clear that the trace without MW radiation does not show any oscillations at low magnetic fields, yet with MW irradiation the R_{xx} vs B shows a set of oscillations in which at certain magnetic fields the R_{xx} goes to zero, i.e., $R_{xx} \to 0$. It is found that these characteristic magnetic fields can be expressed as [11]

$$B = \left[\frac{4}{4j+1}\right] B_f \tag{3.1}$$

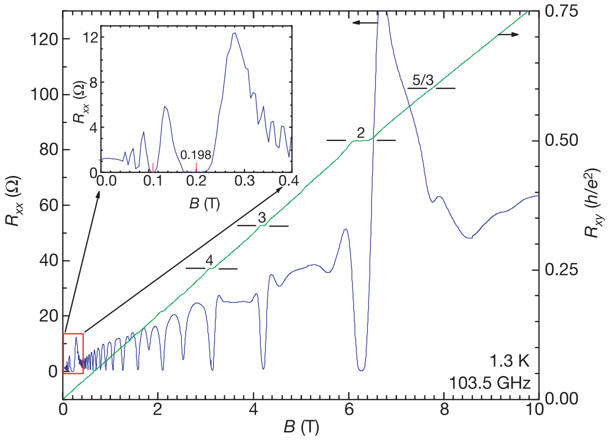

Figure 3.1 The first observation of radiation induced zero resistances on high-mobility GaAs/AlGaAs heterostructure devices at 103.5 GHz. Quantum Hall effects occur at high B as $R_{xx} \to 0$. Inset shows an expanded view of the low-B data where $R_{xx} \to 0$ in the vicinity of 0.198 Tesla under microwave excitation. After Mani et al. (2002).[11]

where $j = 1, 2, \ldots$, and

$$B_f = \frac{2\pi f m^*}{e}. \tag{3.2}$$

Further a close inspection of the Hall effect in the vicinity of these MW induced ZRS, unlike IQHE and FQHE, is not accompanied by a Hall plateau.[11]

3.2 Microwave induced magnetoresistance oscillations

After the initial discovery of MW induced ZRS, there have been an increasing interest in the field of radiation induced magneto-transport and a lot of research has been done both experimentally [11, 16, 20–24, 27, 28, 32, 35, 37–39, 64–70] and theoretically [40, 41, 43, 47, 48, 50, 51, 55, 59, 62, 72, 73, 75–80] in order to understand the physics of MIMO. This section will review the experimental work has been done in this field and the next section, section 3.3, will discuss the theoretical developments on understanding the physics of MW induced ZRS and MIMO in 2DES.

It is already mentioned that the magnetic fields at which the ZRS appear scale with the MW frequency f, effective mass m^* and the electronic charge e [eq. (3.1) and eq. (3.2)]. The frequency dependence of the ZRS is shown in Figure 3.3. At low frequencies the MIMO

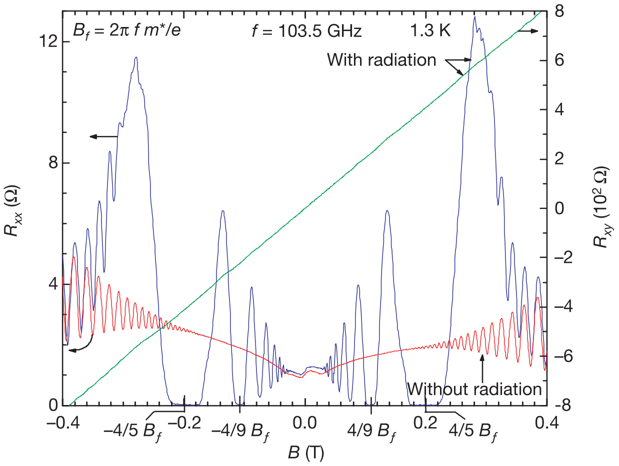

Figure 3.2 R_{xx} and R_{xy} vs B with and without microwave radiation at 103.5 GHz. Unlike in the QHE, there are no Hall plateaus observed when the $R_{xx} \to 0$ under microwave excitation. After Mani et al. (2002).[11]

can be observed only upto about 0.25 Tesla and does not overlap with SdH oscillations [see Figure 3.3 (a)]. On the other hand at higher frequencies MIMO extends to higher magnetic fields as expected; consequently, it overlaps with SdH oscillations [see Figure 3.3 (b)].[11, 22, 29, 31]

Microwave power, DC current, and temperature dependence of MIMO are shown in Figure 3.4 (a), (b), and (c), respectively. The amplitude of the MW induced magnetoresistance oscillations appear to be increasing with the MW power and ultimately the resistance minima reach zero [see Figure 3.4 (a)]. Later it has found that MIMO amplitude is proportional to the square root (non-linear) of the MW power P, i.e., MIMO amplitude $\propto \sqrt{P}$.[13, 37] Furthermore, there are other reports indicating that MIMO amplitude is linear in MW power.[16, 50] According to the ref. [11] MIMO are not sensitive to the DC current passing through the specimen [see Figure 3.4 (b)]. Temperature dependence of MW induced ZRS as well as MIMO have been studied, and Figure 3.4 (c) illustrates that the temperature dependence of a ZRS near $4/5B_f$ and MIMO at lower magnetic fields.[11] It can clearly be seen that as the temperatures increases MIMO amplitude become smaller and smaller.

Rather interesting phenomenon have been observed at higher frequencies as the MIMO and MW induced ZRS overlap with SdH oscillations[11, 22, 29, 31] and quantum Hall ef-

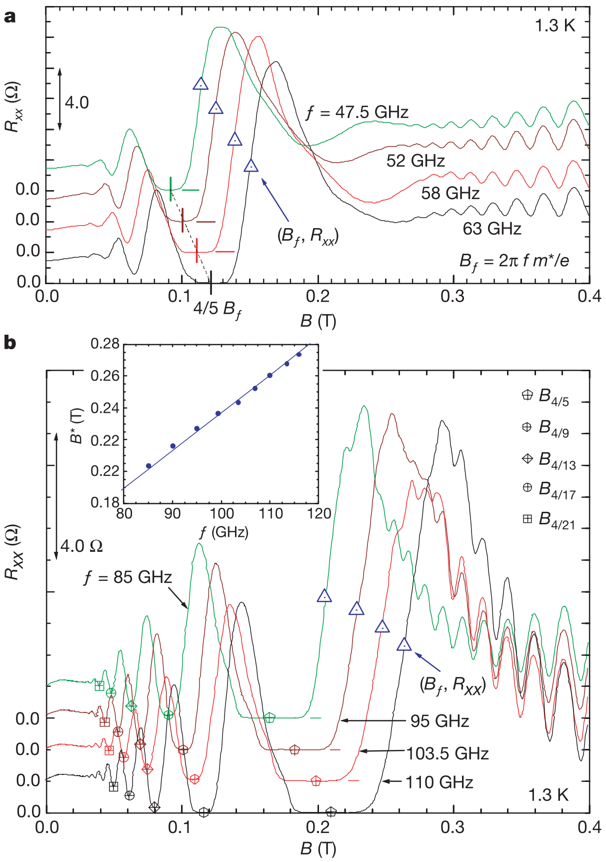

Figure 3.3 Development of microwave induced zero resistance state for different frequencies. After Mani et al. (2002). [11]

fects.[36] Under quantum Hall effects conditions a plateau in the Hall effect have been observed as the resistance reach zero (see section 2.5, and section 2.6). As the MW induced ZRS at higher frequencies overlap with quantum Hall plateaus at higher filling factors, it has been reported that the Hall plateau disappear as MIMO reach zero resistance.[36] In other words, photoexcitation replace the IQHE with ordinary (classical) Hall effect. The reason for this kind of behaviour is yet to be understood.

3.3 Physical origin of microwave induced magnetoresistance oscillations

Microwave induced zero-resistance states appear when the associated B^{-1}-periodic magnetoresistance oscillations grow in amplitude and become comparable to the dark resistance of the 2DES. Such oscillations, which exhibit nodes at cyclotron resonance and harmonics

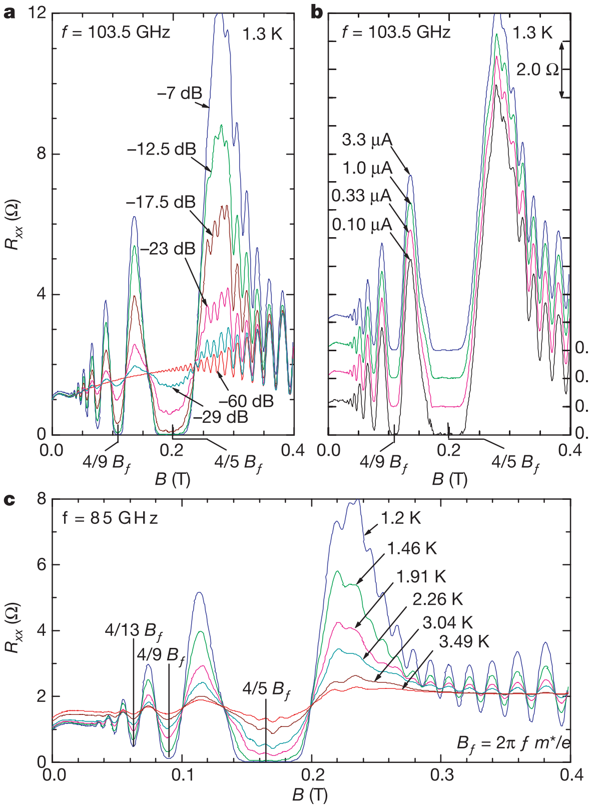

Figure 3.4 (a) Microwave power, (b) DC current, and (c) temperautre dependence of MIMO. After Mani et al. (2002). [11]

thereof,[64, 65] are now understood via the the displacement model,[40, 43, 72, 77] the non-parabolicity model,[73] the inelastic model,[50, 75] and the radiation driven electron orbit model.[47, 48, 51, 76] In theory, some of these mechanisms can drive the magnetoconductivity to negative values at the oscillatory minima. Negative conductivity then triggers an instability in favor of current domain formation, and zero-resistance states.[41, 59] Following sections will provide a brief overview for some of these models.

3.3.1 Displacement model

Several theoretical approaches have been reported[40, 43, 72, 77] in order to describe the behaviour of MIMO in 2DES that are based on displacement model. Here, this section will briefly describe the theory by Durst et al.[40] in order to illustrate the basic idea of the theories based on displacement model. In the presence of MW radiation, electron absorbs a

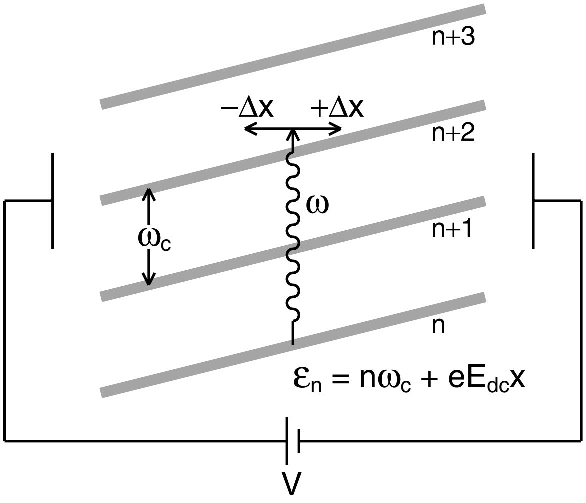

Figure 3.5 Simple illustration of radiation induced disorder assisted current is shown. Adopted from ref. [40].

photon and excited by an energy $\hbar\omega$.

$$\omega = 2\pi f \tag{3.3}$$

where f is the MW frequency. In the presence of disorder these excited electrons can be scattered and hence the conductivity will be modified. Application of a DC bias will result in a finite tilt in the Landau levels (see Figure 3.5). Photoexcited electrons can move to the left (positive bias) or right (negative bias) by a distance of Δx after scattering by a disorder depending on ω and ω_c. If the density of states to the left is greater than that of to the right then the DC current will enhanced and if the density of states to the left is less than that of to the right then the DC current will reduced. Consequently, oscillations in the conductivity can be manifested in the photoexcited specimen.[40] According to this theory, the observed radiation induced magnetoresistance oscillation can be explained considering only the disorder assisted scattering in the presence of MW radiation. According to the authors, numerical simulations using the theoretical model are in good agreement with the experimental observations reported in ref. [11] regarding the phase and the period of the oscillations. Furthermore, the authors also predict that, in theory, the phase observed in experiments[11] is not universal and it can vary from 0 to 1/2 depending on the disorder and the intensity, yet the nodes observed at integer values of ω/ω_c appeared to be insensitive to these parameters. According to the displacement model the photon assisted acoustic phonon scattering is responsible for the experimentally observed temperature dependence of the radiation induced magnetoresistance oscillations amplitude.[72]

3.3.2 Inelastic model

Within this theory the magnetoresistance oscillations induced by the microwave radiation is governed by a change in the electron distribution function induced by MW radiation.[50, 75] Since the density of states relate to the Landau quantization and it is an oscillatory function of B^{-1}, the correction to the electron distribution function includes a oscillatory structure as well. As a result, this will generate a contribution to the DC conductivity that oscillates with ω/ω_c. Here the dominant contribution to the effect comes from inelastic scattering, mainly electron-electron scattering, and therefore the effect is strongly temperature dependent. Furthermore, the magnitude of the effect increases with the decreasing temperature as T^{-2} for $k_BT \gg \hbar\omega$ and as T^{-1} for $k_BT \ll \hbar\omega$.[50, 75] Also according to the theory, the MW induced effect is linear in MW power for not too strong power levels. Although the theory has been developed considering only the linearly polarized MW radiation, the results are predicted to be the same for circularly polarizaed radiation away from $\omega = \omega_c$. In addition, it also predicts insensitivity to the orientation of the MW field, yet the recent experimental results suggests otherwise [70, 71]; see Chapter 5 for more details about the experimental results on polarization dependence of MIMO.

3.3.3 Radiation driven electron orbit model

The radiation driven electron orbit model [47, 48, 51, 76] is based on a perturbation treatment for elastic scattering due to charged impurities to an exact solution for the harmonic oscillator wave function under MW radiation. In the absence of MW radiation, the electron orbits are fixed and the electrons jump between the orbits upon scattering from charged impurities. In the theoretical model, the authors consider a 2DES subjected to a magnetic field applied along the z-axis and a DC electric field along the x direction, which is responsible for the transport through the 2DES. In addition, the system is subjected to a AC electric field E_{MW} due to linearly polarized MW radiation. The linearly polarized MW radiation is characterized by the polarization angle α,

$$\tan\alpha = \frac{E_y}{E_x} \tag{3.4}$$

where E_x and E_y are the respective amplitudes of the MW field E_{MW} along x and y directions. In such a situation the average distance advanced by the electron ΔX^{MW} in each scattering event can be written as,

$$\Delta X^{MW} = \Delta X^0 + A\cos(\omega\tau) \tag{3.5}$$

where ΔX^0 is the average distance advanced by an electron in the absence of MW radiation and $A\cos(\omega\tau)$ is the distance advanced due to MW radiation. Here ω and τ are the MW frequency and impurity scattering time, respectively.[76] The amplitude A of the average distance advanced due to MW radiation is given by [76]

$$A = \frac{eE_0}{m^*\sqrt{\frac{\omega^2(\omega_c^2-\omega^2)^2}{\omega^2\cos^2\alpha+\omega_c^2\sin^2\alpha}+\gamma^4}}. \tag{3.6}$$

Here E_0 is the MW field intensity and γ is a sample dependent parameter, which has a significant effect on the motion of MW driven electron orbits and hence the MW induced effects. According to eq. (3.6), for $\gamma > \omega$ the value of γ dominates over the other terms and the value of A become independent of α, i.e., for $\gamma > \omega$ the MW induced effect is independent of the direction of the linearly polarized MW radiation. On the other hand, if $\gamma < \omega$ the polarization angle α dependent term dominates, and hence the effect become polarization dependent. Polarization direction dependence of MW induced resistance oscillations is discussed in great detail in Chapter 5.

The temperature dependence of the MW induced oscillations is related to γ. According to the theory, increasing temperature will damp ΔX^{MW}, and thereby reducing the oscillation amplitude. Further, the authors propose that electron acoustic-phonon interactions as a possible explanation for the temperature dependence of the MW induced effect.[47, 48]

3.3.4 Non-parabolicity model

The non-parabolicity model considers a classical model for transport in a 2DES under applied a magnetic field normal to the 2D plane and under strong irradiation.[73] Near cyclotron resonance, i.e., $\omega = \omega_c$, in the presence of linearly polarized MW radiation, the electron spectrum demonstrates a weak non-parabolicity, and this will cause a small change in the electron effective mass. Consequently, this gives rise to a change in the diagonal conductivity, but not in the transverse voltage, giving rise to MIMO. Further, in this theory, the MIMO only occurs for linearly polarized MW radiation, and not for circularly polarized MW radiation. The effect of MW radiation on the diagonal conductivity depends on the orientation between the DC electric field and MW electric field; consequently, the non-parabolicity model also predicts a polarization dependence for MIMO.[73] Even though the model can predict the MW induced oscillations in the diagonal conductivity near cyclotron resonance, experimentally observed oscillations in the vicinity of the harmonics of the cyclotron resonance cannot be modeled [11] in the context of the model given in ref. [73].

Thus far we discussed the experimental and theoretical work done in the past to investigate the properties of the MIMO observed in high quality 2DES. It is clear that the existing theoretical models differ in their opinion about the dependence of MIMO on physical parameters, such as temperature, polarization, power, etc. In the following chapters, Chapter 4, and Chapter 5, we will present the experimental work that has been done towards understanding the physics of MIMO in terms of heating due to MW radiation and polarization dependence.

CHAPTER 4

MICROWAVE INDUCED ELECTRON HEATING

4.1 Introduction

In chapter 3, section 3.1 and section 3.2 already discussed the experimental and theoretical work that has been done towards understanding the physics of MIMO. As has been shown in the experiments, the energy absorption rate is small in high-mobility electron systems at low temperatures. However, this does not imply a negligible electron heating, since the electron energy-dissipation rate is also small because of weak electron-phonon scattering at low temperatures. Indeed, theory has [45, 49, 51], in consistency with common experience, indicated the possibility of microwave induced electron heating in the high mobility 2DES in the regime of the radiation induced magnetoresistance oscillations. Not surprisingly, under steady state microwave excitation, the 2DES can be expected to absorb energy from the radiation field. At the same time, electron-phonon scattering can serve to dissipate this surplus energy onto the host lattice [49]. Lei et al. [49] have determined the electron temperature, T_e, by balancing the energy dissipation to the lattice and the energy absorption from the radiation field, while including both intra-Landau level and inter-Landau level processes. In particular, they showed that the electron temperature, T_e, the longitudinal magnetoresistance, R_{xx}, and the energy absorption rate, S_p, can exhibit remarkable correlated non-monotonic variation vs ω_c/ω, where ω_c is the cyclotron frequency [eq. (2.14)], and ω is the radiation frequency [eq. (3.3)].[49] Under these circumstances, it would be interesting to investigate experimentally the possibility of electron heating due to microwave radiation in a regime where microwave induced magnetoresistance oscillations are observable. In such a situation, some questions of experimental interest are: (a) How to probe and measure electron heating in the microwave-excited 2DES? (b) What is the magnitude of electron heating under typical experimental conditions? (c) Finally, is significant electron heating a general characteristic in microwave radiation induced transport?

4.2 Effect of MW radiation on SdH oscillation amplitude

The SdH oscillation amplitude shows strong sensitivity to the electron-temperature.[49] Consequently, an approach to the characterization of electron-temperature or possibility of heating due to MW radiation could involve a study of the amplitude of the SdH oscillations, which also occur in R_{xx} in the photo-excited specimen. Typically, SdH oscillations are manifested at higher magnetic fields, B, than the radiation induced magnetoresistance oscillations, i.e., $B > B_f = 2\pi f m^*/e$, eq. (3.2), especially at low microwave frequencies, say $f \leq 50$ GHz at $T \geq 1.3$ K. On the other hand, at higher f, SdH oscillations can extend into the radiation induced magnetoresistance oscillations. In a previous study, Mani et al. [31] has reported that the SdH oscillation amplitude scales linearly with the average background resistance in the vicinity of the radiation induced resistance minima, indicating the SdH oscillations vanish in proportion to the background resistance at the centers of the radiation induced zero-resistance states. In ref. [29], the authors discuss damping of SdH oscillations and a strong suppression of magnetoresistance in a regime where microwaves induce intra-Landau-level transitions. Kovalev et al. [22] have reported the observation of a node in the SdH oscillations at relatively high-f. Both ref. [31] and ref. [22] examined the range of $\omega_c/\omega \leq 1$, whereas ref. [29] examined the $\omega_c/\omega \geq 1$ regime.

Lei et al. have suggested, in a theoretical study, that a modulation of SdH oscillation amplitude in R_{xx} when the 2DES is subjected to irradiation results from electron heating caused by the radiation in a region where there is no overlapping of SdH oscillations and MIMO.[49] Furthermore, they have shown that, in $\omega_c/\omega \leq 1$ regime, both T_e and S_p exhibit similar oscillatory features, while in $\omega_c/\omega \geq 1$ regime, both T_e and S_p exhibit a relatively flat response.

Here, we investigate the effect of microwaves on the SdH oscillation amplitude over $2B_f \leq B \leq 3.5B_f$, i.e., $2\omega \leq \omega_c \leq 3.5\omega$. In particular, we compare the relative change in the SdH oscillation amplitude due to lattice temperature changes in the dark (w/o MW radiation), with the changes in the SdH amplitude under microwave excitation at different microwave power levels and frequencies (at a constant temperature). The change in the electron temperature ΔT_e due to MW radiation can be extracted. In good agreement with theory, the results indicate $\Delta T_e \leq 50$ mK over the examined regime.

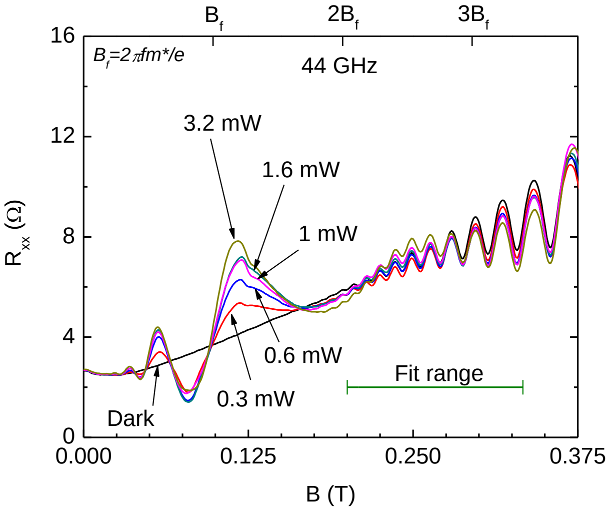

Figure 4.1 Microwave induced magnetoresistance oscillations and SdH oscillations in R_{xx} are shown at 1.5 K for 44 GHz at different power levels P. A horizontal marker (green) shows the field range ($2B_f \leq B \leq 7/2B_f$) where SdH fits were carried out.

The lock-in based electrical measurements, Appendix B, were performed on Hall bar devices fabricated from high quality GaAs/AlGaAs heterostructures. Experiments were carried out with the specimen mounted inside a waveguide and immersed in pumped liquid helium, see Appendix B for further details. The frequency spanned $25 \leq f \leq 50$ GHz at source power levels $P \leq 5$ mW. Magnetic-field-sweeps of R_{xx} vs P were carried out at 1.6 K at 41.5 GHz, and at 1.5 K at 44 GHz and 50 GHz.

Microwave induced magnetoresistance oscillations can be seen in Figure 4.1 at $B \leq 0.175$ Tesla, as strong SdH oscillations are also observable under both the dark and irradiated conditions for $B \geq 0.2$ Tesla. Over the interval $2B_f \leq B \leq 3.5B_f$, where the SdH oscillations are observable, one could observe small variations in the background R_{xx} at higher power levels in comparison to the dark trace, see Figure 4.2. Thus, a smooth R_{xx} background,

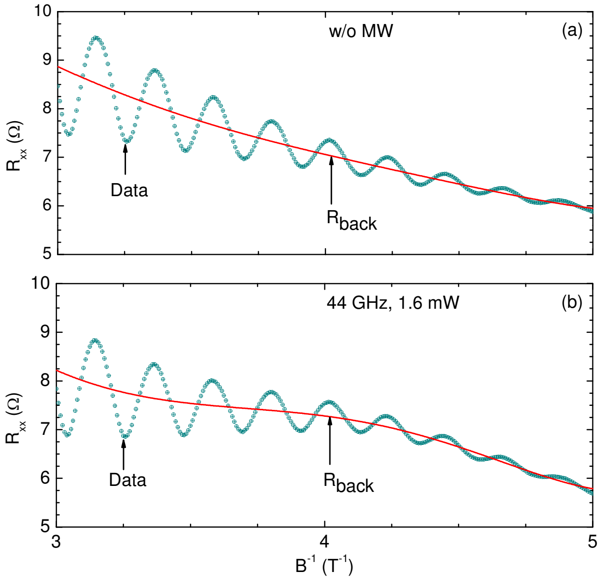

Figure 4.2 Small variations in the SdH oscillations background (a) w/o and (b) w/ MW radiation are shown. R_{back} is a NLSF to a order 5 polynomial, which represent the backbround variations in SdH oscillations.

R_{back}, was subtracted from the magnetoresistance data,

$$\Delta R_{xx} = R_{xx} - R_{back}. \tag{4.1}$$

Figure 4.3 (a)-(f) shows the background subtracted R_{xx}, i.e., ΔR_{xx}, measured without [Figure 4.3 (a)] and with [Figure 4.3 (b)-(f)] microwave radiation versus the inverse magnetic field B^{-1}. To extract the amplitude of the SdH oscillations, we performed a standard Nonlinear Least Squares Fit (NLSF) on ΔR_{xx} data with an exponentially damped sinusoid,

$$\Delta R_{xx} = -Ae^{-\frac{\alpha}{B}} \cos\left(\frac{2\pi F}{B}\right) \tag{4.2}$$

Here, A is the amplitude, F is the SdH frequency, B is the magnetic field, and α is the damping factor. The fit results for the dark-specimen ΔR_{xx} data are shown in the Figure 4.3 (a) as a solid line. This panel suggests good agreement between data and fit in the dark condition. Similarly, we performed NLSFs of the ΔR_{xx} SdH data taken with the microwave

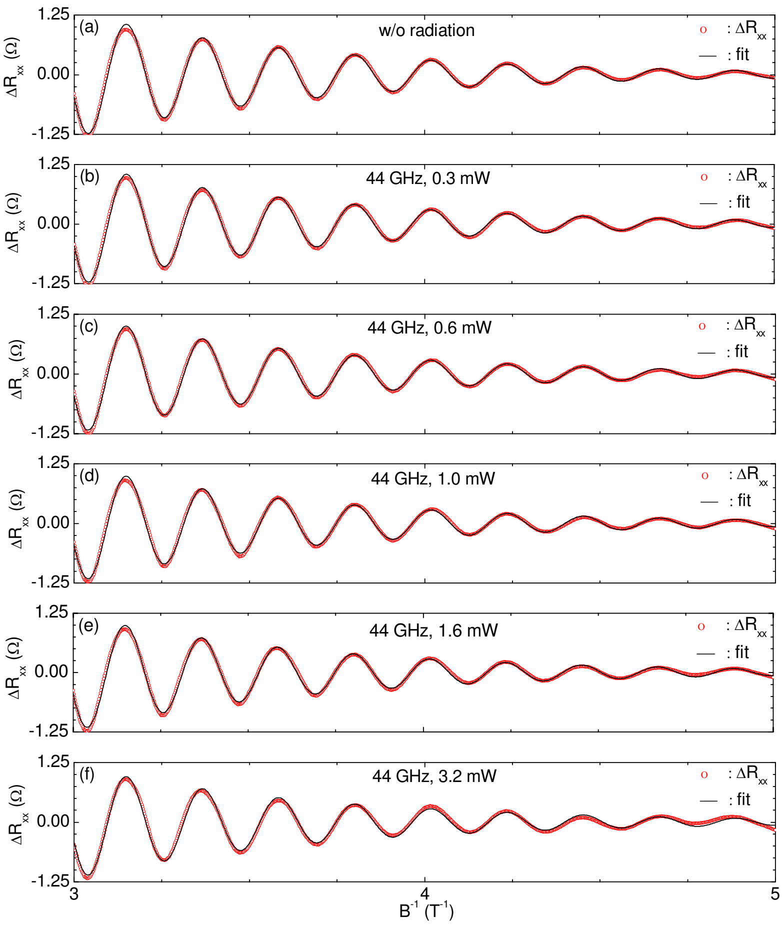

Figure 4.3 (a) The background subtracted R_{xx}, i.e., ΔR_{xx}, in the absence of radiation (open circles) and a numerical fit (solid line) to eq. (4.2) are shown here. Panels (b)-(f) show the ΔR_{xx} and the fit at the indicated P.

power spanning approximately $0 \leq P \leq 3$ mW, see Figure 4.3 (b)-(f). The parameters α and F are insensitive to the incident radiation at a constant temperature, consequently, we can fix α and F to the dark-specimen constant values. In Figure 4.3, panels (b)-(f) show the $T = 1.5$ K ΔR_{xx} data (open circles) and fit (solid line) obtained with $f = 44$ GHz for different MW power levels. The SdH oscillations amplitude A extracted from the NLSFs are exhibited vs the microwave power in Figure 4.4. Here, A decreases with increasing microwave power. Our analysis of other power-dependent data (see Figure 4.7) yielded similar results.

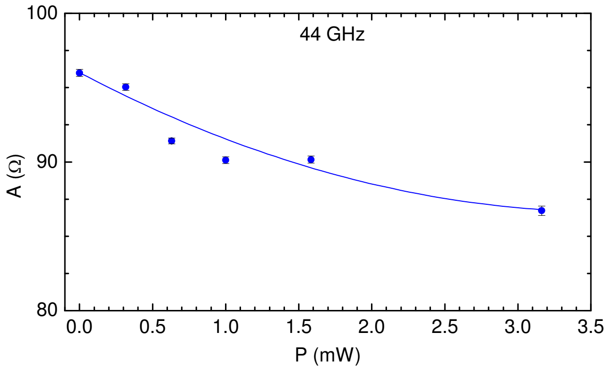

Figure 4.4 MW power dependence of the SdH amplitude A at 44 GHz.

4.3 Temperature dependence of SdH oscillation amplitude

Next, we examine the influence of temperature on the SdH oscillation amplitude. Figure 4.5 shows R_{xx} vs B with the temperature as a parameter. It is clear [see the dashed (black) lines in Figure 4.5] that increasing the temperature rapidly damps the SdH oscillations at these low magnetic fields. In order to extract the SdH oscillation amplitude from these data, we used the same fitting model, see eq. (4.2), as described previously. But, for the T-dependence analysis, α was separated into two parts, α_{T_0} and $\beta\Delta T$,

$$\alpha = \alpha_{T_0} + \beta\Delta T \tag{4.3}$$

since we plan to relate the change in the SdH oscillation amplitude for a temperature increment to the observed change in the SdH amplitude for an increment in the microwave power at a fixed f. Here α_{T_0} represents the damping at the base temperature, T_0, and $\beta\Delta T$ is the additional damping due to the temperature increment,

$$\Delta T = T - T_0. \tag{4.4}$$

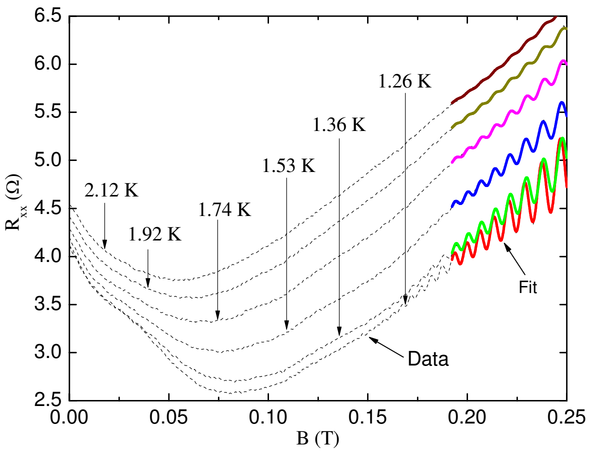

Figure 4.5 Temperature (T) dependence of R_{xx} is shown for $1.26 \leq T \leq 2.12$ K. The dashed (black) lines show the data, and the thick-solid (colored) lines indicate the fits.

Substituting α from eq. (4.3) into eq. (4.2) yields

$$\Delta R_{xx} = -Ae^{-\left(\frac{\alpha_{T_0}+\beta\Delta T}{B}\right)} \cos\left(\frac{2\pi F}{B}\right) \tag{4.5}$$

which gives

$$\Delta R_{xx} = -A'e^{-\frac{\alpha_{T_0}}{B}} \cos\left(\frac{2\pi F}{B}\right) \tag{4.6}$$

where

$$A' = Ae^{-\frac{\beta\Delta T}{B}}. \tag{4.7}$$

Here A' represents the change in the SdH oscillation amplitude due to a change in temperature ΔT. Note that the parameters α_{T_0} and F can be extracted from the R_{xx} fit at the lowest T and set to constant values. Data fits made with eq. (4.6) are included in Figure 4.5 as thick-solid (colored) lines. Thus, the NLSF served to determine A' at each temperature. Figure 4.6 shows the temperature dependence of A', while the inset of Figure 4.6 shows a semi-log plot of A' vs T. The inset confirms an exponential dependence for A' on T, see eq. (4.7).

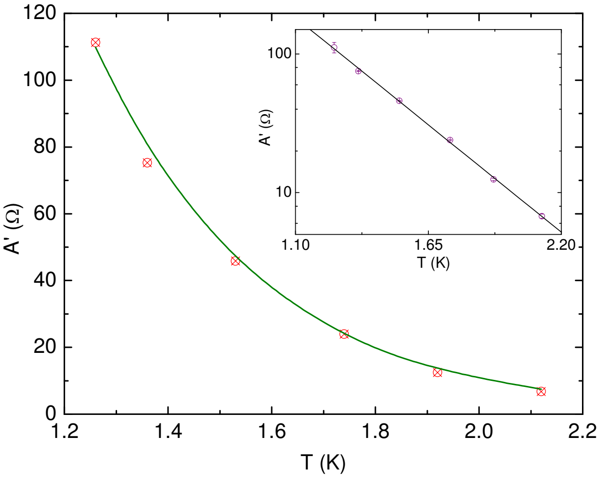

Figure 4.6 The exponential variation of the amplitude A' with T is shown. The inset confirms that $\log(A')$ is linear in T.

4.4 Effect of MW radiation on electron temperature

Experiments indicate that increasing the source-power monotonically decreases the SdH oscillation amplitude at the examined frequencies including 44 GHz (see Figure 4.4), 50 GHz and 41.5 GHz (see Figure 4.7). Since increasing the temperature also decreases the SdH oscillation amplitude (see Figure 4.5, and Figure 4.6), one might extract the electron temperature change under microwave excitation by inverting the observed relationship between A' and T,

$$\Delta T = -\frac{B}{\beta}\left(\ln A' + c\right) \tag{4.8}$$

where β is a constant. Thus, the dark measurement of the SdH oscillation amplitude vs the temperature serves to calibrate the temperature scale vs the SdH oscillation amplitude, and the slope of the solid line in Figure 4.8 (a) reflects the inverse slope of Figure 4.6. Also plotted as solid symbols in Figure 4.8 (a) are the A under microwave excitation at various frequencies and power levels. Here, one can see that the change in SdH oscillation amplitude induced by microwave excitation over the available power range is significantly smaller than the change in SdH oscillation amplitude induced by a temperature change of 0.9 K. By transforming the observed change in A between minimum- and maximum- power at each f to a ΔT_e, we

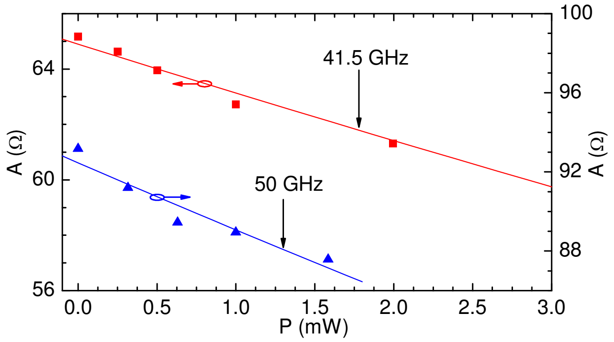

Figure 4.7 Variation of A with P is shown for $f = 41.5$ GHz (left axis) and $f = 50$ GHz (right axis).

can extract the maximum ΔT_e induced by photo-excitation at each f, and this is plotted in Figure 4.8 (b). Although the power at the sample can vary with f, even at the same source power, Figure 4.8 (b) indicates that the maximum ΔT_e scales approximately linearly with the peak source microwave power [see Figure 4.8 (b) solid guide line]. Furthermore, from Figure 4.8 (b), it appears that $\Delta T_e/\Delta P = 9$ mK/mW.

4.5 Discussion and Summary

According to theory [45, 49, 51] steady state microwave excitation can heat a high mobility two-dimensional electron system. The energy gain from the radiation field is balanced by energy loss to the lattice by electron-phonon interaction. In ref. [49], Lei et al. suggest that longitudinal acoustic (LA) phonons provide greater contribution to energy dissipation than the transverse acoustic (TA) phonons in the vicinity of $T = 1$ K in the GaAs/AlGaAs system, if one neglects the surface or interface phonons. At such low temperatures and modest microwave power, away from the cyclotron resonance condition, where the resonantly absorbed power from the microwave radiation is not too large and the electron temperature remains well below about 20 K, the longitudinal optical (LO) phonons do not influence the resistivity since the energy scale associated with LO-phonons is large compared to the energy scale for acoustic phonons. Within their theory, Lei et al. [49] show that the electron temperature follows the absorption rate, exhibiting rapid oscillatory behavior at low B, i.e.,

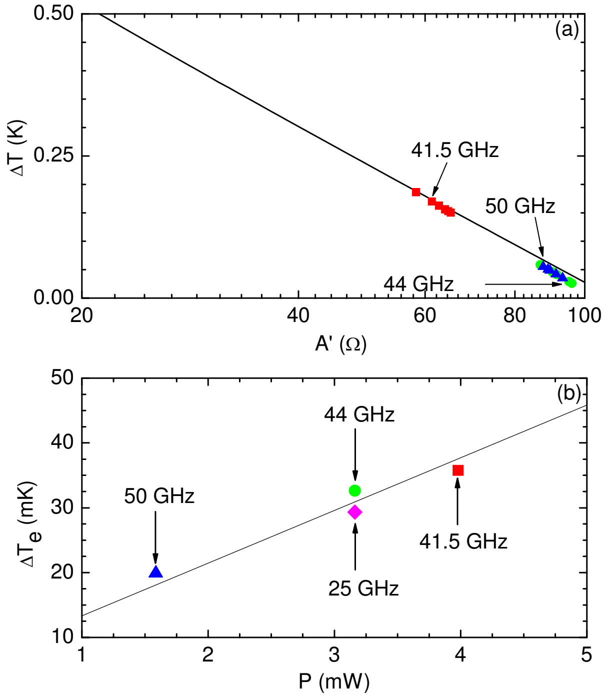

Figure 4.8 (a) The effects of T and P on A' (solid line) and A (solid symbols) are shown here. Corresponding T-change was determined through the exponential relation between ΔT and A'. Panel (b) shows a plot of maximum ΔT_e vs peak-P (solid symbols), with a line to guide the eye.

$\omega_c/\omega \leq 1$, followed by slower variation at higher B, i.e., $\omega_c/\omega \geq 1$. Indeed, even at the very high microwave intensities, P/A, e.g. $4 \leq P/A \leq 18$ mW/cm^2 at 50 GHz, the theory does not show a significant change in the electron temperature for $B \geq 2B_f$ except at $P/A \geq 10.5$ mW/cm^2. Thus, theory indicates that the electron temperature is nearly the lattice temperature in low P/A limit especially for $B \geq 2B_f$, i.e., $\omega_c \geq 2\omega$. In comparison, in these experiments, the source power satisfied $P \leq 4$ mW, with $A \approx 1$ cm^2, while the power at the sample could be as much as ten times lower due to attenuation by the hardware. Remarkably, we observe strong microwave induced resistance oscillations (see Figure 4.1) in the $B \leq B_f$ regime at these low intensities. The results, see Figure 4.8 (c), indicate just a small rise, $\Delta T \leq 50 \times 10^{-3}$ K, in the electron temperature T_e, above the lattice temperature T. Apparently, in the spirit of the Lei et al. theory [49], the electron heating is negligible here because energy absorption rate is rather small over the investigated regime.

In summary, the experimental study carried out to investigate the possibility of electron heating in 2DES due to MW radiation indicates that the change in electron temperature is relatively small over the regime $2\omega \leq \omega_c \leq 3.5\omega$ based on the effect of MW radiation on the SdH oscillation amplitude in comparison with that of the temperature, when the microwave excitation is sufficient to induce strong microwave induced resistance oscillations, in good agreement with theoretical predictions.

CHAPTER 5

POLARIZATION SENSITIVITY OF MW INDUCED MAGNETORESISTANCE OSCILLATIONS

5.1 Introduction

The theoretical models that describe the physics of radiation induced magnetoresistance oscillations diverge in their opinion on polarization sensitivity of the radiation induced magnetoresistance oscillations. The displacement model predicts that the amplitude of the oscillations depends on whether the linearly polarized microwave electric field E_ω is parallel or perpendicular to the *dc*-electric field E_{DC}.[72] Furthermore, according to the theory, the inter-Landau level contribution to the photo-current includes a term with a Bessel function whose argument depends upon whether E_ω and E_{DC} are parallel or perpendicular to each other. In addition, the Bessel function argument remains a constant for unpolarized or circular polarized radiation for any ratio of ω_c/ω.[72] According to the radiation-driven electron orbit model polarization immunity depends upon the damping factor, γ,- a material- and sample-dependent parameter, exceeding the microwave frequency, ω, i.e., $\gamma > \omega$.[47, 48, 76] In the case of $\gamma < \omega$, however, the radiation-driven electron orbit model would indicate a sensitivity of MIMO to the relative orientation of linearly polarized E_ω and E_{DC}. Within the non-parabolicity theory, only the linearly polarized, but not circularly polarized, microwave radiation is capable of producing the microwave induced magnetoresistance oscillations.[73] As a result, the radiation induced contribution within this theory also depends on the relative orientation between E_{DC} and the linearly polarized E_ω.[73] The inelastic model, however, suggests insensitivity of the photoconductivity to the polarization orientation of the linearly polarized microwave field.[50, 75]

There have been several attempts to investigate, experimentally, the polarization aspect of the MIMO.[20, 21, 28] The investigations carried out on devices with square geometry in a quasioptical setup report that the microwave induced magnetoresistance oscillations and zero resistance states are insensitive to the sense of circular and linear polarizations.[28] On the other hand, measurements carried out on L-shaped specimens have suggested that the phase and period of the microwave induced magnetoresistance oscillations are insensitive to the configurations of $E_\omega \parallel I$ and $E_\omega \perp I$.[20, 21] Under these circumstances a systematic study of polarization sensitivity of microwave induced magnetoresistance oscillations will be helpful for further improving the understanding of the physics of radiation induced transport in 2DES.

In this study, the polarization sensitivity of microwave induced magnetoresistance oscillations has been investigated by rotating the polarization direction of the linearly polarized microwave radiation relative to the Hall bar device.[70, 71] Surprisingly, at low microwave power, P, experiments indicate a strong sinusoidal response as $R_{xx}(\theta) = A \pm C\cos^2(\theta - \theta_0)$ vs the polarization rotation angle, θ, with the plus $(+)$ and minus $(-)$ cases describing the maxima and minima, respectively. At higher P, the principal resistance minimum exhibits additional extrema vs θ. Further the results also indicate that the phase shift θ_0 can vary with f, B, and $\mathrm{sgn}(B)$.[71]

5.2 Polarization direction of the linearly polarized MWs

Rotating the direction of the linearly polarized microwaves relative to a fixed axis is not an easy task, and these polarization-dependence studies utilized the novel setup illustrated in Figure 5.1 (a) (see also appendix A.1.1). Here a rotatable MW-antenna introduces microwaves into a circular waveguide with 11 mm inside diameter.

Due to circular symmetry the rotation of the MW-antenna allows us to rotate the polarization of the MW electric field with respect to the stationary sample, see Figure 5.1 (a) and Figure 5.1 (b). The transverse electric (TE) mode excited by the MW-antenna shown in Figure 5.1 (a) would excite a TE_{11} mode in the circular waveguide; consequently, the specimen will be subjected to the TE_{11} mode of the circular waveguide as shown in Figure 5.1 (c). The scaled sketches of the small (400 μmm wide) Hall bar specimen within

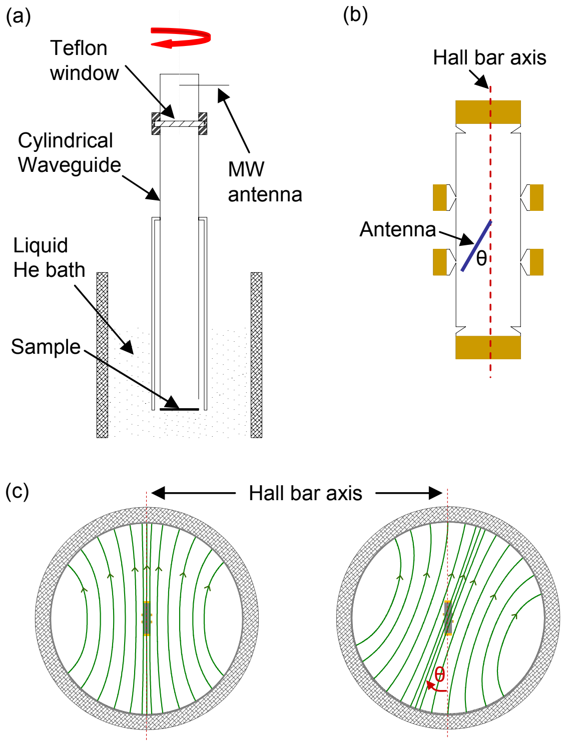

Figure 5.1 (a) A microwave (MW) antenna is free to rotate about the axis of a cylindrical waveguide. (b) A Hall bar specimen, shown as "sample" in (a), is oriented so that the Hall bar long-axis is parallel to the MW-antenna for $\theta = 0°$. (c) This scaled figure shows the TE_{11} mode electric field pattern within the waveguide with the Hall bar superimposed on it. The left panel illustrates $\theta = 0°$ case, while the right panel shows the finite θ case. Note the parallel electric field lines within the active area of the specimen.

the waveguide (11 mm i.d.), with superimposed electric field lines shown in Figure 5.1 (c) suggest that the polarization is well defined over the active area of the specimen for all rotation angles.

The specimens investigated in these studies consisted of 400 μm wide Hall bars characterized by n (4.2 K) $= 2.2 \times 10^{11}$ cm^{-2} and $\mu \approx 8 \times 10^{6}$ cm^2/V s. The long axis of these Hall bars were visually aligned parallel to the polarization axis of the MW-antenna and this defined $\theta = 0°$. Consequently, the angle θ represents the polarization rotation angle, see Figure 5.1 (b) and Figure 5.1 (c).

Now it is important to test whether the polarization is preserved through the waveguide. The test consisted of following steps. First, the measurements were carried out with the MW-

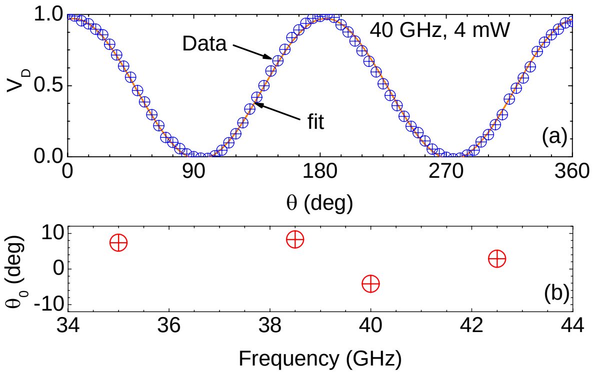

Figure 5.2 (a) Normalized detector response vs the polarization angle is shown for 40 GHz. (b) The phase shift obtained from NLSFs for different frequencies.

antenna [Figure 5.1 (a)] connected directly to the MW analyzer, a probe-coupled antenna together with a square law detector, and the results indicated that polarized microwaves were generated by the MW-antenna. Second, the waveguide sample holder was inserted between the MW-antenna and the analyzer. In this step the analyzer was set at a fixed orientation, and the MW-antenna was rotated over 360° (see appendix A.1.1 for more detail). The results indicate that the polarization is preserved through the cylindrical waveguide, and the Figure 5.2 exhibits the expected sinusoidal variation, i.e., $V_D \propto \cos^2\theta$, for linearly polarized radiation, as a function of θ. The normalized detector response, V_D, at $f = 40$ GHz is shown in Figure 5.2 (a). Also shown in Figure 5.2 (a) is a fit to $V_D = A + C\cos^2(\theta - \theta_0)$, eq. (A.1), that is used to extract θ_0. Figure 5.2 (b) shows the variation of θ_0 with the MW frequency, f, with the analyzer in place of the specimen. According to the Figure 5.2 (b), $\theta_0 \leq 10°$ for $34 \leq f \leq 44$ GHz. This result shows that the polarization at the sample location follows the expected behavior within an experimental uncertainty of approximately 10 degrees.

5.3 Microwave induced magnetoresistance oscillations vs polarization angle

Figure 5.3 exhibits the R_{xx} vs B at frequencies (a) 35.5, (b) 37, and (c) 39 GHz with power $P = 0.32$, 0.16, and 0.63 mW, respectively, with the Hall bar sample in place at the bottom of the waveguide of the sample holder. Each panel of Figure 5.3 includes three lines.

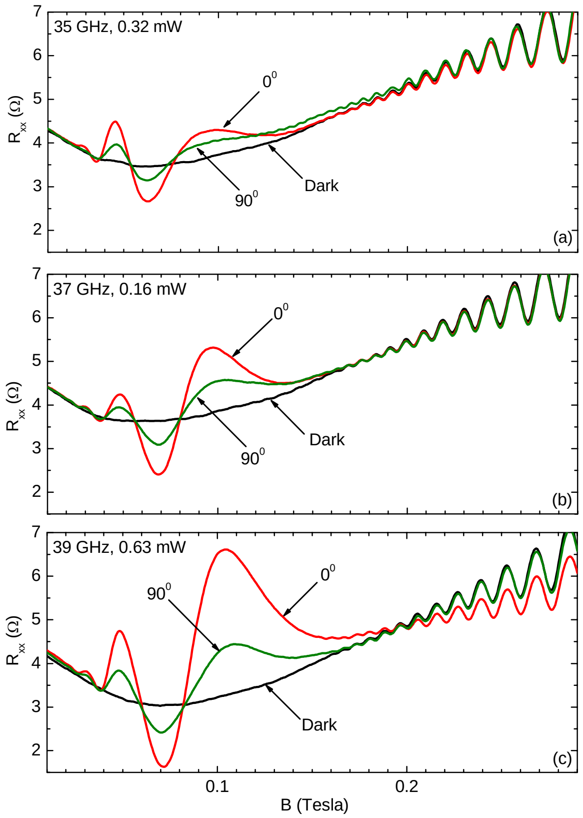

Figure 5.3 (a) Microwave induced magnetoresistance oscillations in R_{xx} are shown at (a) $f = 35$ GHz, (b) 37 GHz, and (c) 39 GHz at 1.5 K. Each panel shows a set of three traces: a dark (w/o MW) curve, a curve obtained at $\theta = 0°$, and a trace obtained at $\theta = 90°$. A clear change in radiation induced oscillations can be seen at different polarization angles.

The first is a dark trace obtained in the absence of microwave photoexcitation. A second trace shows the result with the MW-antenna parallel to the long axis of the Hall bar, i.e., $\theta = 0°$. These exhibit nice microwave induced magnetoresistance oscillations for all three frequencies at the respective power levels. Finally, each panel of Figure 5.3 also exhibits a trace for the case where the MW-antenna is perpendicular to the long axis of the Hall bar, i.e., $\theta = 90°$. Again, these traces also exhibit good microwave induced magnetoresistance oscillations for all three frequencies at the same power levels.

A remarkable feature is observed when one compares the traces at $\theta = 0°$ and $90°$ within any single panel of Figure 5.3. The amplitude of the microwave induced magnetoresistance oscillations is reduced at the $\theta = 90°$ MW-antenna orientation, i.e., the amplitude of the microwave induced magnetoresistance oscillations has been reduced when the MW E-field is perpendicular to the long axis of the Hall bar compared to when the MW E-field is parallel to the long axis of the Hall bar. Although the magnetoresistance oscillations are reduced in amplitude, typically, they are not completely damped at $\theta = 0^\circ$.[70] Here, it is worth noting that the period and the phase of the radiation induced magnetoresistance oscillations appear not to be influenced by θ [11, 20, 21, 64], although the amplitude of the oscillatory response is strongly sensitive to it; this feature is readily apparent in Figure 5.3.

5.3.1 MIMO amplitude vs polarization angle

A remarkable feature of this setup is that one can rotate the polarization direction of the linearly polarized microwaves 360° with respect to a fixed direction. Consequently, it allows us to study the variation of the MIMO amplitude as function polarization angle θ at a fixed magnetic field. Figure 5.4(a) shows the dark- and photo-excited- diagonal resistance R_{xx} vs B. Here, the photo-excited measurement was carried out with microwave frequency $f = 39$ GHz and microwave power $P = 0.32$ mW, and the MW-antenna parallel to the Hall bar long-axis, i.e., $\theta = 0^\circ$. Aside from the well developed MIMO in Figure 5.4 (a), one can also see a well-known negative magnetoresistance to $B = 0.075$ Tesla in the high mobility specimen in the dark condition.[68] In Figure 5.4 (a), the labels $P1$, $V1$, and $P2$, identify the oscillatory extrema that are examined in Figure 5.4 (b), (c), and (d), respectively. Figure 5.4 (b) and (d) show that the photoexcited R_{xx}, i.e., "w/ MW", traces lie above the dark, i.e., "w/o MW", R_{xx}, traces at the resistance maxima for all θ. Further, the photo-excited R_{xx} at $P1$ and $P2$ fits the function

$$R_{xx}(\theta) = A + C\cos^2(\theta - \theta_0) \tag{5.1}$$

with $\theta_0 = -6.7^\circ$ and -1.6°, respectively. Figure 5.4 (c) shows that at the resistance minimum $V1$, the "w/ MW" R_{xx} trace lies below the dark R_{xx} for all θ as it follows

$$R_{xx}(\theta) = A - C\cos^2(\theta - \theta_0) \tag{5.2}$$

with $\theta_0 = -8.4°$. Thus, the greatest radiation-induced R_{xx} oscillatory response occurs when the antenna is approximately parallel or anti-parallel to the Hall bar long-axis.[70]

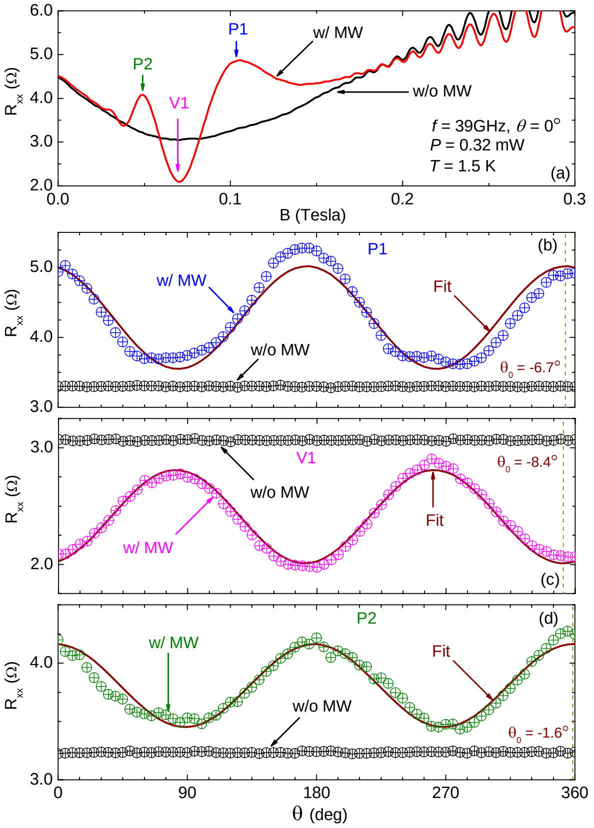

Figure 5.4 (a) The dark- and microwave excited- magnetoresistance R_{xx} are exhibited. Here the microwave antenna is parallel to the long axis of the Hall bar, i.e., $\theta = 0°$. The principal maxima have been labelled $P1$ and $P2$, and the minimum is $V1$. (b), (c), and (d) show the experimental extremal R_{xx} response at $P1$, $V1$, and $P2$, respectively. (b) and (d) show that, at the maxima $P1$ and $P2$, R_{xx} under photoexcitation exceeds the dark R_{xx}. On the other hand, at $V1$, the R_{xx} under photoexcitation lies below the dark R_{xx}.

Next we compare experimental results obtained under magnetic field reversal. Figure 5.5 (a) shows R_{xx} vs B with $f = 40$ GHz over the B-range $-0.25 \leq B \leq 0.25$ Tesla. These data are exhibited to compare the relative angular response at extrema in positive and negative side of the magnetic field B. As in Figure 5.4 (a), extrema of interest have been labelled in Figure 5.5 (a), here as $P^{+}1$, $V^{+}1$ and $P^{+}2$ for those in the domain $B > 0$, and $P^{-}1$, $V^{-}1$ and $P^{-}2$ for the extrema in the domain $B < 0$. It can be easily seen that $R_{xx}(\theta)$ response illustrates a sinusodal behaviour at all the respective extrema in both sides of the magnetic field as expected. Furthermore, as in Figure 5.4, the angular response of the extrema can be fit with eq. (5.1) and eq. (5.2) for maxima and minima, respectively.

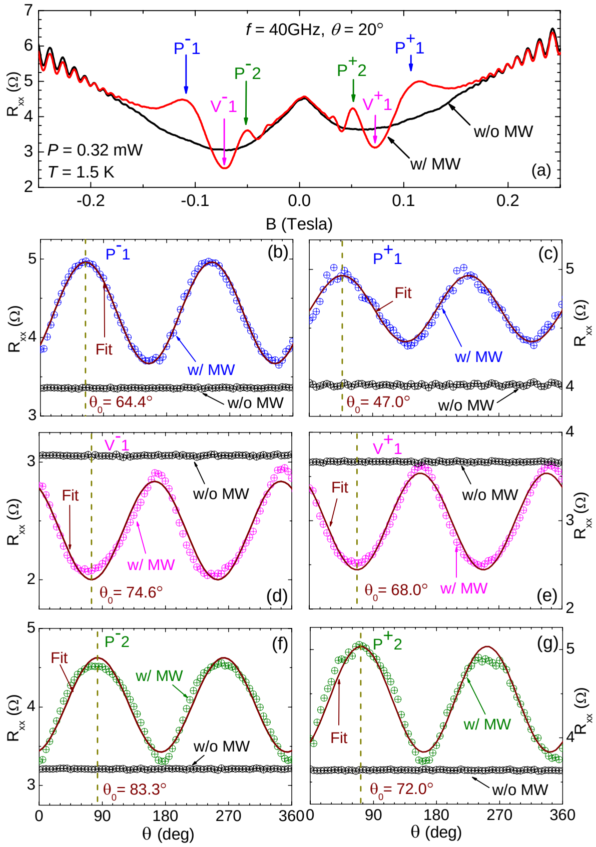

Figure 5.5 This figure compares the angular response for positive and negative magnetic fields. (a) Dark- and photo-excited- R_{xx} are shown at $f = 40$ GHz with $\theta = 20^\circ$ over the B-range $-0.25 \leq B \leq 0.25$ Tesla. (b), (d), and (f) show the θ dependence of R_{xx} of the principal maxima $P^{-}1$ (b), $P^{-}2$ (f), and the minimum $V^{-}1$ (d) for $B < 0$. (c), (e), and (g) show the θ dependence of R_{xx} of the principal maxima $P^{+}1$ (c), $P^{+}2$ (g), and the minimum $V^{+}1$ (e) for $B > 0$. In these figures, the w/o MW traces indicate the sample response in the dark, while the w/ MW traces indicate the response under photo-excitation. The phase shift, θ_0, is indicated by a vertical dashed line in (b)-(g).

However, the fit extracted θ_0 differs substantially from zero, well beyond experimental uncertainty. Indeed, a close inspection suggests that θ_0 depends upon the extremum in question, i.e., B, and the orientation of the magnetic field, i.e., sgn(B). For example, we find that $\theta_0 = 64.4^\circ$ for $P^{-}1$ and $\theta_0 = 47^\circ$ for $P^{+}1$. Such a large difference in θ_0 due to magnetic field reversal is unexpected. Note that since the MW antenna is far from the magnet and well isolated from the magnetic field, the magnetic field is not expected to influence the polarization of the microwaves at launch. Furthermore, the stainless steel microwave waveguide is not known to (and we have also not seen it) provide a microwave frequency, magnetic field, and magnetic field orientation dependent rotation to the microwave polarization. Thus, the θ_0 shift depending on B and $\text{sgn}(B)$ appears to be a sample effect.

5.4 Power dependence of $R_{xx}(\theta)$ response

Now it is already clear that the MIMO amplitude is extremely sensitive to the orientation of the linearly polarized MW E-field relative to the long axis of the Hall bar.[71] Also, we learned that the fit extracted θ_0 is dependent on B, and $\text{sgn}(B)$. In this situation it is important to examine the role of the microwave power in the polarization sensitivity. Figure 5.6(a) exhibits, for $f = 37$ GHz, R_{xx} vs B with $P = 0.32$ mW, along with the dark curve. At the principal maximum $P1$ and the principal minimum $V1$, we examine the variation of R_{xx} with θ, for different microwave power levels P. Figure 5.6(b) shows R_{xx} vs θ at $P1$ with $P = 0.32, 1.0$, and 3.16 mW, and Figure 5.6(c) shows the same at $V1$ for the respective power levels. Note that $\theta_0 = 37°$ for $P1$ here at $f = 37$ GHz, which differs from the $\theta_0 = -6.7°$ for $P1$ observed at $f = 39$ GHz [see Figure 5.4], and $\theta_0 = 47°$ for $P^{+}1$ at $f = 40$ GHz [see Figure 5.5]. Yet, Figure 5.6 (b) shows that the θ_0 does not change with the microwave power, P. At $P = 0.32$ mW in Figure 5.6 (c), R_{xx} exhibits a simple sinusoidal variation at the principal minimum $V1$ as in Figure 5.4 and Figure 5.5. However, at $P = 3.16$ mW, new peaks appear in Figure 5.6 (c) [but not in Figure 5.6 (b)], in the vicinity of $\theta = 45°$ and $\theta = 225°$, where none were evident in the $P = 0.32$ mW trace.

The emergence of these extra peaks is unexpected. Perhaps this could be understood in the context of better coupling of the electric field of the MW radiation with the 2DES at certain alignments. For an example, as shown in Figure 5.6 (b) and (c), MWs at $f = 37$ GHz create a coupling that is stronger near $\theta = 45°$ and $\theta = 225°$ as the amplitude of MIMO reaches maximum amplitude around these angles. Furthermore, increase of the magnitude of

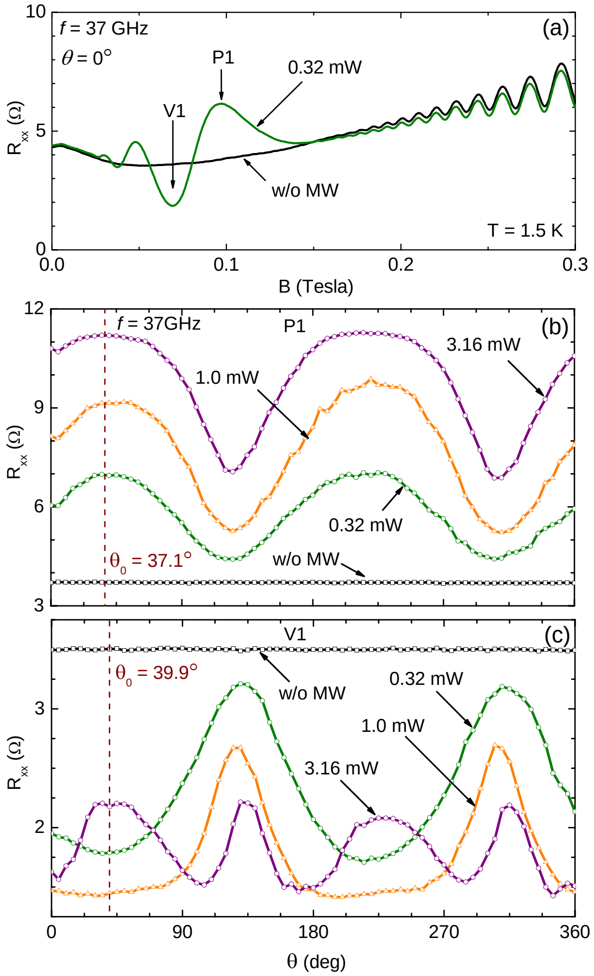

Figure 5.6 This figure examines the angular response of R_{xx} at different microwave power levels, P. (a) Magnetoresistance oscillations in R_{xx} are exhibited for $f = 37$ GHz with $\theta = 0$ and $P = 0.32$ mW. (b) shows the θ dependence of R_{xx} of the principal maximum $P1$. (c) shows the θ dependence of R_{xx} of the principal minimum $V1$. In these figures, the w/o MW (w/ MW) traces indicate the sample response in the absence (presence) of microwave photo-excitation. Note that, in (c), additional peaks occur near $\theta = 45°$ and $\theta = 225°$ at $P = 3.16$ mW.

the MW electric field, especially at these angles, can possibly overdrive the electronic system into a breakdown condition where the amplitude of radiation induced magnetoresistance oscillations actually shrink with the increasing magnitude of the electric field of the MW radiation.

5.5 $R_{xx}(\theta)$ response at spatially distributed contacts

The data exhibited above showed that the phase shift, θ_0 can vary with f, B, and the sign of B, and yet it does not depend on the the MW power. Next we report results obtained on either sides of the Hall bar device, and compare θ_0 obtained by measuring the angular dependence of R_{xx}. Note that these measurements were carried out on a Hall bar device oriented perpendicular to the microwave antenna at the outset. Thus, the starting angle for R_{xx} vs θ measurements is $-90°$ [see Figure 5.7]. At the top of Figure 5.7, the dark- and photo-excited- $R_{xx}(B)$ response of the left side of the Hall device, R^L_{xx} [see Figure 5.7 (a)] and the right side of the Hall bar device, R^R_{xx} [see Figure 5.7 (b)] are shown at $f = 43$ GHz with $P = 0.5$ mW and $\theta = -90°$. Here, once again, $\theta = -90°$ indicates that the MW-antenna is perpendicular to the long axis of the Hall bar. The R^L_{xx} vs θ traces for $f = 43$ GHz and $P = 0.32$ mW at the first ($P1$) and second ($P2$) maxima are shown in Figure 5.7 (c) and (g), respectively. Similarly, the R^R_{xx} vs θ traces for $f = 43$ GHz and $P = 0.32$ mW at $P1$ and $P2$ are shown in Figure 5.7 (d) and (h), respectively. According to Figure 5.7 (c) and (d), the fit extracted θ_0 for R^L_{xx} and R^R_{xx} are 8.9° and 1.6°, respectively, at $P1$, and they are $-5.2°$ and $-5.3°$, respectively, at $P2$. Also, the R_{xx} vs θ at $V1$ for either sides of the sample [Figure 5.7 (e) and (f)] reveal that $\theta_0 = 1.7°$ for R^L_{xx} and $\theta_0 = -0.5°$ for R^R_{xx}. Comparison of the θ_0 values at different extrema on both sides of the Hall bar device indicates that the values are similar for both sides of the device within the experimental uncertainty, see Figure 5.2(b).

5.6 Discussion and Summary

In this chapter I present the first experimental evidence for the observation of the sensitivity of microwave induced magnetoresistance oscillations to the polarization direction

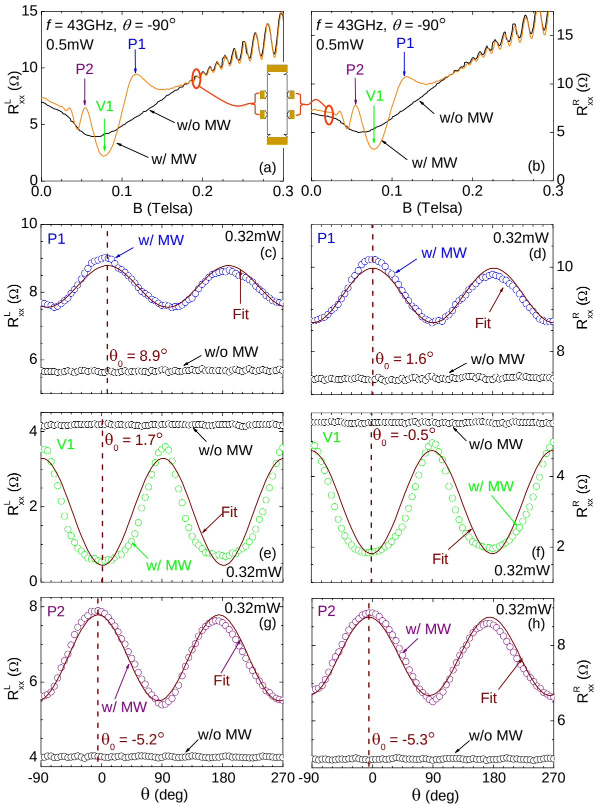

Figure 5.7 This figure exhibits the angular dependence of the diagonal resistance on the left and right sides of the Hall bar device, see panel (a) inset. Dark- and photo-excited- R_{xx} is shown for the (a) left side, R^L_{xx}, and (b) right side, R^R_{xx}, at $f = 43$ GHz with $P = 0.5$ mW and $\theta = -90°$. Panels (c), (e), and (g) show the θ dependence of the R^L_{xx} for $P = 0.32$ mW at the first maximum ($P1$), first minimum ($V1$), and second maximum ($P2$), respectively. Similarly, panels (d), (f), and (h) show the θ dependence of the R^R_{xx} for $P = 0.32$ mW at $P1$, $V1$, and $P2$, respectively. Phase shifts obtained for the two sides of the Hall bar, R^L_{xx} and R^R_{xx}, show similar values within the experimental uncertainty at $f = 43$ GHz.

of the linearly polarized microwaves.[70, 71] The main features are:

(a) At low P, $R_{xx}(\theta) = A \pm C\cos^2(\theta - \theta_0)$ vs the linear polarization rotation angle, θ, with the plus (+), eq. (5.1), and minus (−), eq. (5.2), cases describing the oscillatory maxima and minima, respectively, see Figure 5.4, Figure 5.5, Figure 5.6, and Figure 5.7.

(b) The phase shift in the $R_{xx}(\theta)$ response, i.e., θ_0, varies with f, B, and the sign of B (compare Figure 5.4, Figure 5.5, and Figure 5.6). Yet, θ_0 appears to be insensitive to the microwave power (see Figure 5.6).

(c) At higher radiation power, the principal resistance minimum exhibits additional extrema vs θ [see Figure 5.6 (c)].

Point (a) demonstrates a strong sensitivity in the radiation induced magnetoresistance oscillations to the sense of linear microwave polarization, in qualitative agreement with the radiation driven electron orbit model when $\gamma < \omega = 2\pi f$ [47, 48, 76]. Such sinusoidal variation of the amplitude of the radiation induced magnetoresistance oscillations could also be consistent with the non-parabolicity model [73] (see fig. 1 of Ref. [73]). As already mentioned, the displacement model also suggests a linear polarization sensitivity.[72] Consequently, the polarization angle dependence reported here can be considered to be consistent with the displacement model as well. Yet, the experimental feature that the oscillations do not vanish completely at $\theta = 90°$ [see, for example, Figure 5.3, Figure 5.4 (b), (c), and (d)] seems not to rule out the existence of a linear-polarization-immune-term in the radiation-induced transport. Points (b) and (c) mentioned above are also interesting. One might also try to understand point (b), for example, in the displacement model. Here, polarization sensitivity [72] is due to the inter-Landau level contribution to the photo-current. In these experiments, the orientation of E_ω is set by the antenna within the uncertainty indicated in Figure 5.2 (b). The orientation of E_{DC} is variable and set by the B-dependent Hall angle, $\theta_H = \tan^{-1}(\sigma_{xy}/\sigma_{xx})$, with respect to the Hall bar long-axis. If a particular orientation between E_ω and E_{DC} is preferred, say, e.g. $E_\omega \perp E_{DC}$ or $E_\omega \ // \ E_{DC}$, for realizing large radiation-induced magnetoresistance oscillations, and the Hall angle changes with B, then a non-zero θ_0 and a variation in θ_0 with B might be expected. However, the observed variations in θ_0 seem much greater than expectations since $\theta_H \approx 90°$ in this regime. The change in θ_0 upon B-reversal is also unexpected, and this feature identifies a possible reason for the asymmetry in the amplitude of R_{xx} under B-reversal often observed in such experiments. Consider the typical R_{xx} vs B measurement sweep, which occurs at a fixed θ. If peak response occurs at different θ_0 for the two field directions, then the oscillatory R_{xx} amplitudes would not be the same for positive and negative B. The observed θ_0 -variations seem to suggest an effective microwave polarization rotation in the self-response of the photoexcited

Hall bar electron device. Since $\theta_0 \approx \pi/4$ (see Figure 5.5 and Figure 5.6), $B \approx 0.1$ Tesla, and the thickness of the 2DES lies in the range of tens of nanometers, such a scenario would suggest giant effective polarization rotation in this high mobility 2DES.[74] Perhaps such results might be understandable in a theory that provides a greater role for magneto-plasmons.[78]

Finally, we reconcile our observations with other reports on this topic.[28, 35] Smet et al. in ref. [28] reported circular and linear polarization immunity in the radiation-induced magneto-resistance oscillations. Their measurements were carried out on 4×4 mm^2 square shaped specimens, with width-to-length ratio of one.[28] In such a square shaped specimen with point contacts, the current stream lines are expected to point in different directions over the face of the sample. Then the variable angle between the linear microwave polarization and the local current orientation could possibly serve to produce an effectively polarization averaged measurement, leading to apparent linear polarization immunity. Ref. [35] examined the interference of magneto-inter-subband oscillations and the microwave radiation-induced magnetoresistance oscillations, and suggested a polarization immunity in the observed interference effect. Since the effect examined by Wiedmann et al. [35] differs substantially from the conventional radiation-induced magnetoresistance oscillations, we think that there need not be an obvious contradiction that needs to be addressed here. At the same time, we note that some experimental details, such as sample geometry and the method for changing the polarization, are needed to make a further meaningful comparison. Finally, measurements carried out on L-shaped specimens [20, 21] led to the conclusion that the phase and the period of the microwave induced magnetoresistance oscillations are independent of the relative orientation of the microwave polarization and the current [20, 21], and this observation is consistent with the initial report [11] and the results reported here.

In summary, experiments identify a strong sinusoidal variation in the diagonal resistance R_{xx} vs θ, the polarization rotation angle, at the oscillatory extrema of the microwave radiation-induced magnetoresistance oscillations.[40, 47, 48, 72, 73, 76] The phase shift θ_0 for maximal oscillatory R_{xx} response under photoexcitation appears dependent upon the radiation frequency f, the extremum in question B, and the magnetic field orientation $\mathrm{sgn}(B)$.[71]

The results provide new evidence for the linear polarization sensitivity in the amplitude of the radiation induced magnetoresistance oscillations.[70, 71]

CHAPTER 6

ELECTRICAL TRANSPORT IN HIGHLY ORIENTED PYROLYTIC GRAPHITE (HOPG)

6.1 Introduction

Single layers of carbon atoms known as graphene are considered to be a strong contender as a material of interest for future electronics.[83–86] At the same time, graphene is a novel 2DES with remarkable features providing for a solid state realization of quantum electrodynamics, massless Dirac particles, an anomalous Berry's phase,[87–89] and an unconventional quantum Hall effect in a strong magnetic field.[83–89] The $ABAB$ bernal stacking of graphene helps to produce graphite, an anisotropic electronic material exhibiting a large difference between the in-plane and perpendicular transport. Since graphite may be viewed as stacked graphene, one wonders whether remnants of the remarkable properties of graphene might also be observable in graphite.

Graphite exhibits a ≈ 0.03 eV band overlap, in contrast to the zero-gap in graphene.[90–92] In the recent past, concepts proposed for graphene have also been invoked for graphite. For example, Luk'yanchuk et al. [93] argues for the observation of massive majority electrons with a three dimensional (3D) spectrum, minority holes with a two dimensional (2D) parabolic massive spectrum, and majority holes with a 2D Dirac spectrum. Hall plateaus in σ_{xy} extracted from van-der-Pauw measurements on highly oriented pyrolytic graphite (HOPG) have been cited as evidence for the integral quantum Hall effect (IQHE) in graphite in ref. [94]. Luk'yanchuk et al. in ref. [95] suggest simultaneous quantum Hall effects for the massive electrons and massless Dirac holes with Berry's phase of $\beta = 0$ and $\beta = 1/2$, respectively. β is given here in units of 2π. Finally, an angle-resolved photoemission spectroscopy (ARPES) study has reported massless Dirac fermions coexisting with finite mass quasiparticles in graphite.[96]

Plateaus of Hall resistance at $R_{xy} = h/ie^2$ with $i = 1, 2, 3, ...$, eq. (2.34), and $R_{xx} \to 0$ are typically viewed as a characteristic of IQHE in the 2DES (Chapter 2). At the same time, a "thick" specimen consisting of quantum wells separated by wide barriers exhibits plateaus at

$$R_{xy} = \frac{h}{ije^2} \tag{6.1}$$

where j counts the number of layers in the specimen. Indeed, introducing a dispersion in the z-direction does not modify the observability of IQHE.[97] Thus, the IQHE can also be a characteristic of anisotropic 3D systems such as graphite. In graphite, the IQHE can be of the canonical variety or of the unconventional type reported in graphene. In addition, theory has predicted the existence of a single, true bulk 3D QHE in graphite in a large magnetic field parallel to the c-axis at $\sigma_{xy} = (4e^2/\hbar)(1/c_0)$, where $c_0 = 6.7$ Åis the c-axis lattice constant.[98]

Thus, there are reasons for carrying out quantum Hall transport studies in graphite. The possibility of both the canonical and unconventional IQHE in graphite motivates also a study of the Berry's phase. Finally, one wonders whether 3D graphite might also satisfy the resistivity rule observed in 2D quantum Hall systems [eq. (6.4)].

The magnetotransport study of HOPG reported here shows strong oscillations in the Hall resistance, R_{xy}, and SdH oscillations in the diagonal resistance, R_{xx}, while manifesting Hall plateaus at the lowest temperatures. A Fourier transform of the R_{xx} SdH oscillations indicates a single set of carriers, namely electrons, in these HOPG specimens. A Berry's phase analysis of the SdH data suggests that these carriers in graphite are unlike those in GaAs/AlGaAs heterostructures, n-GaAs epilayers, bulk semiconducting $\mathrm{Hg_{0.8}Cd_{0.2}Te}$, the HgTe quantum well, 3D AlGaN, and InSb systems. In addition, a resistivity rule study of graphite indicates $R_{xx} \sim -B \times dR_{xy}/dB$, in variance with observations of canonical quantum Hall systems, while a phase analysis suggests a new classification ("type-IV") [36] of the phase relation between the oscillatory R_{xx} and R_{xy}. The latter observation is consistent with $R_{xx} \sim -B \times dR_{xy}/dB$.

6.2 Hall Effect and the magnetoresistance in HOPG

Our 25 μm thick graphite specimens were exfoliated from bulk HOPG (see Appendix C), and the measurements were carried out using standard lock-in techniques (see Appendix B for further details) with the B parallel to the c-axis. Measurements of R_{xx} and R_{xy} are shown in Figure 6.1 (a) and (b), respectively, for $1.5 \leq T \leq 154$ K and $0 \leq B \leq 5$ T. At low T, SdH oscillations in R_{xx} and R_{xy} and plateaus in R_{xy} appear [see Figure 6.1 (a) & (b), as in Fig.2 and Fig.3 of ref. [100]]. Three Hall plateaus are observable in Figure 6.1 (b). The Hall plateau resistance observed at $B = 2.5$ T and $T = 1.5$ K is consistent, within a factor-of-two, with viewing the specimen as a stack of uncoupled quantum Hall layers. Note that $R_{xx} > 0$ through the Hall plateaus. The finite tilt of the highest-B plateau at $T = 1.5$ K might be due to the incipient R_{xy} saturation, possibly due to multi-band transport.

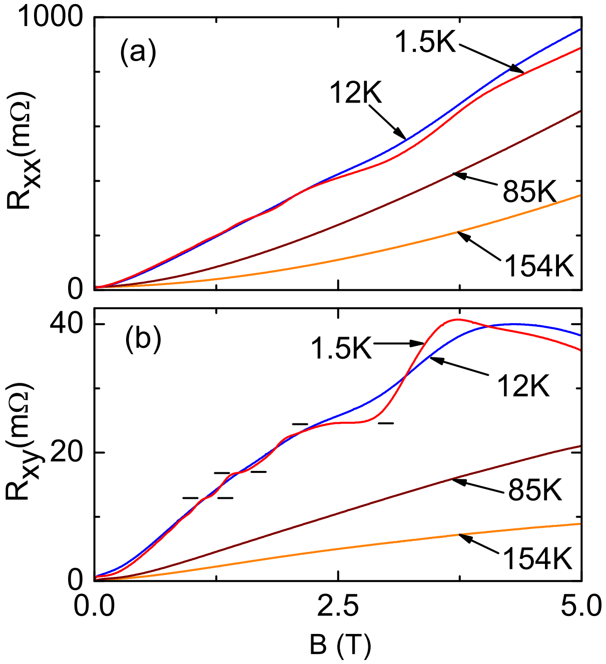

Figure 6.1 (a) The diagonal resistance (R_{xx}) and (b) Hall resistance (R_{xy}) of sample $S1$ are exhibited vs the applied magnetic field, B, between $154 \leq T \leq 1.5$ K. R_{xy} plateaus and SdH oscillations in R_{xx} are manifested at low T.

6.3 SdH oscillations and the Berry's phase

The SdH effect has been used to probe the Berry's phase.[87, 88] For the graphene system, the oscillatory R_{xx}, ΔR_{xx}, can be written as [89]

$$\Delta R_{xx} = R(B,T)\cos\left[2\pi\left(\frac{B_0}{B}+\frac{1}{2}+\beta\right)\right] \tag{6.2}$$

where $R(B,T)$ is the SdH oscillation amplitude and is a functions of the temperature T and the magnetic field B, B_0 is the SdH oscillation frequency, and β is the Berry's phase in units of 2π. The observation of an anomalous Berry's phase in graphene has generated new interest in the study of the same in graphite. Hence, we set out to examine our data for graphite from a similar perspective.

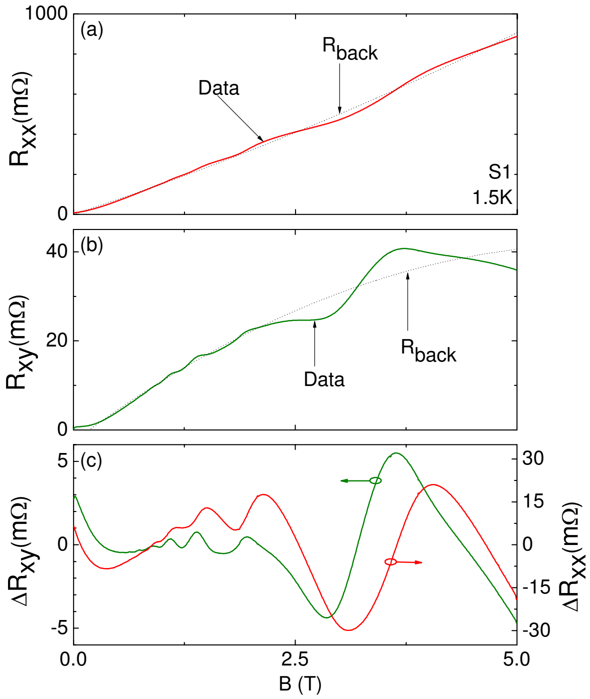

Figure 6.2 Panels (a) and (b) shows the measured data (solid line) for R_{xx} and R_{xy} for $S1$ at 1.5 K and the subtracted background, R_{back}, (dashed line). (c) Background subtracted R_{xx} (right) and R_{xy} (left) are shown.

Graphite is a semi-metal with majority electrons and holes exhibiting elongated Fermi

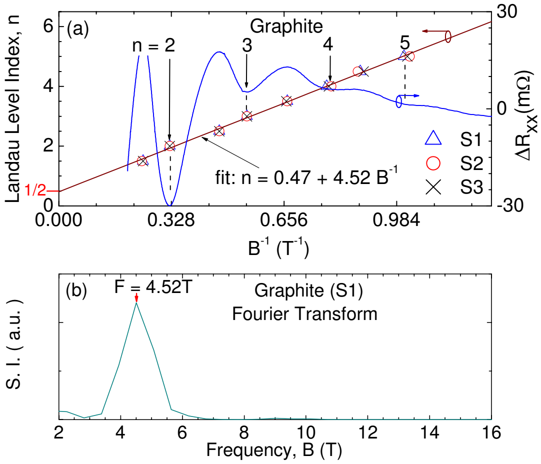

Figure 6.3 (a) Shown here are plots of Landau level index (n)(left) of samples $S1$, $S2$, and $S3$, and R_{xx} (right) of sample $S1$, vs B^{-1}. The slope of the n vs B^{-1} plot indicates SdH frequency, $F = 4.52$ Tesla, and an intercept, $n(B^{-1} = 0) = 0.47$. (b) This plot shows the spectral intensity of the Fourier transform of $\Delta R_{xx}(1/B)$ of sample $S1$. A single peak in the Fourier spectrum confirms that the SdH effect in these graphite specimens is basically dominated by one type of carrier with $F = 4.52$ T.

surfaces along the c-axis.[91] The Fermi surface of graphite has been studied via the oscillatory magnetization (de Haas -van Alphen [dHvA]) effect and also the oscillatory magnetoresistance (SdH) effect.[91] Graphite exhibits a strong dHvA effect, and the Fourier transform of the associated oscillatory magnetization readily exhibits two spectral peaks corresponding to the two sets of majority carriers. The SdH data, on the other hand, can often exhibit just a single broad peak in the Fourier spectrum.[95] It has been suggested that the scattering lifetimes manifested by the carriers in the two experiments might not be the same.[91] Furthermore, one set of carriers might suffer more broadening, and as a consequence, the associated oscillatory contribution due to this band might vanish in the SdH effect.

As has been shown in Figure 6.2, a smooth background, R_{back} - a second order polynomial, was subtracted from the R_{xx} and R_{xy} signals to extract the oscillatory parts of R_{xx} and R_{xy}, namely ΔR_{xx}, ΔR_{xy} [Figure 6.2 (c)]. In order to examine and compare the Berry's phase, plots of the Landau level index, n (left axis), and ΔR_{xx} (right axis) versus B^{-1} are shown in Figure 6.3 (a), and Figure 6.4 (a), (b), and (c) for graphite, the GaAs/AlGaAs 2D electron system, an n-GaAs epilayer[101], and bulk semiconducting $Hg_{0.8}Cd_{0.2}Te$[102],

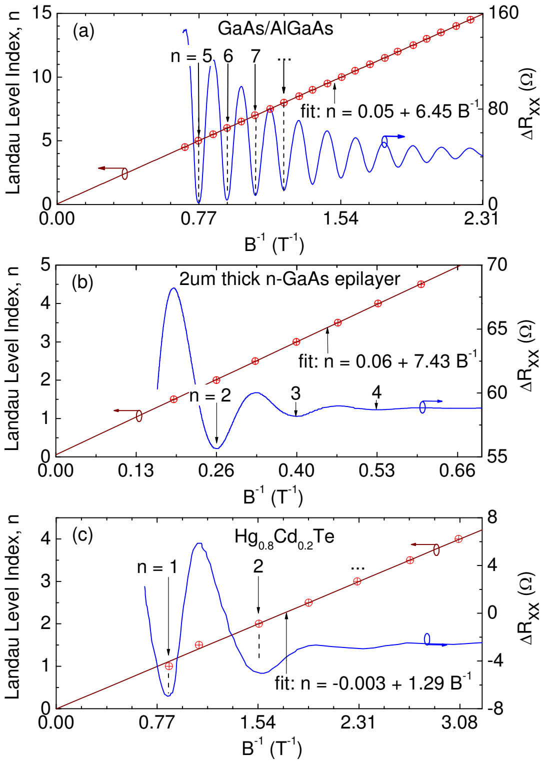

Figure 6.4 (a) n and R_{xx} are shown vs B^{-1} for the GaAs/AlGaAs 2D electron system. In (b) & (c) n and R_{xx} are shown for the 2 μm thick n-GaAs epilayer and 3D $Hg_{0.8}Cd_{0.2}Te$ systems. Linear fit of n vs B^{-1} intersects the ordinate at 0.05, 0.06, and -0.04 for GaAs/AlGaAs, 2 μm thick n-GaAs epilayer, and bulk $Hg_{0.8}Cd_{0.2}Te$ systems, respectively.

respectively. For all four material systems, minima of oscillatory R_{xx} have been assigned with n, and maxima of the oscillatory R_{xx} have been assigned with $n + 1/2$, as in ref. [89]. In such an analysis, an intercept $n_0 = 0$ would normally indicate a Berry's phase $\beta = 0$, while $n_0 = 1/2$ would normally correspond to $\beta = 1/2$, as in graphene.[89] For the three graphite samples $S1$, $S2$, and $S3$, the Landau level index intercept of a linear fit to n vs B^{-1} yields $n_0 = 0.47$, i.e., 1/2 [see Figure 6.3 (a)]. Panels (a), (b), and (c) in Figure 6.4 give intercepts of 0.05, 0.06, and -0.04, i.e., zero, for the GaAs/AlGaAs, n-GaAs epilayer, and bulk $Hg_{0.8}Cd_{0.2}Te$ systems. These fit-extracted intercepts, n_0, and B_0 are summarized in Table 6.1.

A similar analysis was carried out with other data and these results are also summarized in Table 6.1 for the HgTe quantum well[103], 3D AlGaN[104], InSb[96], and $C_{9.3}AlCl_{3.4}$ -

Table 6.1 Intercept n_0 and the slope B_0 of (n) vs B^{-1} plot. β is the suggested Berry's phase.

Material	n_0	B_0 (Tesla)	β
Graphite	0.47 ± 0.02	4.52	1/2
GaAs/AlGaAs	0.05 ± 0.01	6.45	0
GaAs[a][96]	0.06 ± 0.02	7.43	0
$Hg_{0.8}Cd_{0.2}Te$[b][97]	-0.003 ± 0.022	1.298	0
HgTe[c][98]	0.06 ± 0.03	26.14	0
3D AlGaN [99]	-0.01 ± 0.03	35.39	0
InSb [105]	0.05 ± 0.03	19.80	0
$C_{9.3}AlCl_{3.4}$[d][100]	0.48 ± 0.02	11.7	1/2

[a] 2 μm thick n-GaAs epilayer
[b] bulk semiconducting $Hg_{0.8}Cd_{0.2}Te$
[c] n-type HgTe quantum wells
[d] 1st stage graphite intercalation compound

a first stage graphite intercalation compound.[106] Notice that Table 6.1 represents eight different systems, yet only graphite and $C_{9.3}AlCl_{3.4}$ show $n_0 = 1/2$ in the $B^{-1} \to 0$ limit as observed in graphene.[89] This is a principal experimental finding of this work.

Furthermore, the HOPG specimens examined in this study are characterized by a single broad peak in the Fourier transform of the SdH data (ΔR_{xx}) [see Figure 6.3 (b)]. This feature suggests that the SdH effect in our HOPG specimen is also dominated by one type of carrier, namely electrons. Does this experimental finding signify an anomalous Berry's phase for the observed carriers in graphite? If the experimental results shown here in Figure 6.1 had indicated $R_{xy} > R_{xx}$ as in ref. [89], then, certainly, the conclusion would immediately follow that electrons in graphite exhibit an anomalous Berry's phase as in graphene. The fact that Figure 6.1 indicates $R_{xy} << R_{xx}$ complicates the issue since many would reason that $R_{xy} << R_{xx}$ implies $\rho_{xy} << \rho_{xx}$ given the geometrical factors in these graphite specimens,

$$\Delta\sigma_{xx} = \Delta\frac{\rho_{xx}}{\rho_{xx}^2 + \rho_{xx}^2} \simeq \Delta\frac{\rho_{xx}}{\rho_{xx}^2} \sim -\Delta R_{xx}. \tag{6.3}$$

As a result, $\Delta\sigma_{xx} \sim -\Delta R_{xx}$, eq. (6.3), unlike in a conventional QH system, where $\Delta\sigma_{xx} \sim \Delta R_{xx}$ for $\rho_{xy} >> \rho_{xx}$. Therefore, in such a situation $n_0 = 1/2$ in graphite should be taken to indicate normal carriers[95], not Dirac carriers as $n_0 = 1/2$ would indicate a $\beta = 0$ according to the procedure described earlier. Some features should, however, serve as a caution about adopting this line of reasoning. First, strong SdH oscillations, as seen in Figure 6.1, are typically observed only when $\rho_{xy} > \rho_{xx}$, i.e., $\omega\tau > 1$, for the associated carriers. Thus, perhaps, the observation of $R_{xy} << R_{xx}$ in graphite need not imply $\rho_{xy} << \rho_{xx}$. Next, it appears that some experiments on the GaAs/AlGaAs system clearly show that there need not be a simple relation between R_{xx} and ρ_{xx}.[108] Finally, it is also known that certain types of longitudinal specimen thickness variations, density variations, and/or current switching between graphene layers in graphite, can introduce a linear-in-B component into R_{xx} originating from the Hall effect; such an effect can produce experimental observations of $R_{xx} >> R_{xy}$ even in systems that satisfy $\rho_{xx} < \rho_{xy}$. Due to such possibilities in graphite, the results shown Figure 6.3, Figure 6.4 and Table 6.1 could plausibly identify an anomalous Berry's phase for electrons in graphite, and $C_{9.3}AlCl_{3.4}$ [106]. It is noteworthy that a semiconducting $Hg_{0.8}Cd_{0.2}Te$ specimen also exhibits $R_{xx} > R_{xy}$ [102] and yet shows $n_0 = 0$, unlike graphite. Clearly, the experimental finding is unambiguous: the infinite field, i.e., $B^{-1} \longrightarrow 0$, phase extracted from the SdH oscillations for graphite is unlike the results for a number of canonical semiconductor systems (see Table 6.1).

6.4 Relative phase of the oscillations in the Hall- and diagonal- resistances

Next, we examine more closely the phase relation in the oscillations of R_{xx} and R_{xy} since this is a striking feature of the data. Background subtracted measurements of R_{xx} and R_{xy}, i.e., ΔR_{xx} and ΔR_{xy}, are shown in Figure 6.5 (a)-(c), for samples $S1$, $S2$, and $S3$. Thus far, the phase relations between ΔR_{xx} and ΔR_{xy} have been classified into three types in the high mobility GaAs/AlGaAs system.[36] Namely, type-III, where the oscillations of ΔR_{xx} and ΔR_{xy} are approximately 180 degrees out of phase, type-II, where the oscillation of the ΔR_{xx} and ΔR_{xy} are in-phase, and type-I, where the peaks of ΔR_{xx} occur on the low-B side of the ΔR_{xy} peaks, with a $\pi/2$ phase shift. Figure 6.5 shows, however, that the peaks of ΔR_{xx} appear on the high-B side of the ΔR_{xy} peaks, unlike the cases mentioned above. This

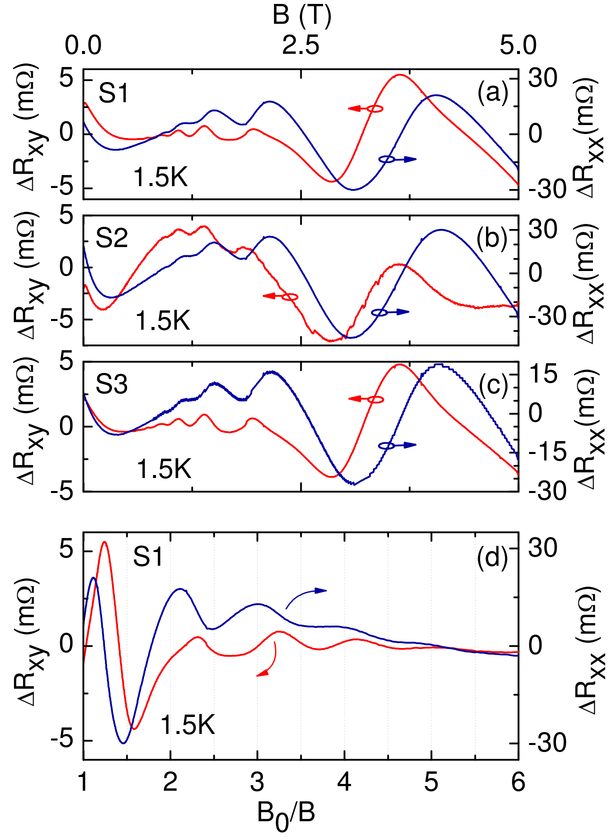

Figure 6.5 The oscillatory Hall- (ΔR_{xy}) and diagonal- (ΔR_{xx}) resistances are shown for samples (a) $S1$, (b) $S2$, and (c) $S3$, vs B. (d) ΔR_{xy} and ΔR_{xx} are shown vs the normalized inverse magnetic field B_0/B. This plot shows a $\pi/2$ phase shift between ΔR_{xx} and ΔR_{xy}.

suggests a fourth phase relation ("type-IV") between ΔR_{xx} and ΔR_{xy} in (HOPG) graphite. In the B^{-1} plot [see Figure 6.5 (d)] the peaks of ΔR_{xx} are shifted towards the low B_0/B side with respect to the peaks of ΔR_{xy}, with an approximately $\pi/2$ phase shift between ΔR_{xx} and ΔR_{xy}, confirming this conjecture.

6.5 Resistivity rule in graphite

The experiments carried out on GaAs/Al$_x$Ga$_{1-x}$As have revealed a remarkable similarity between the Hall resistance and the diagonal resistance.[99] According to Chang et al. [99],

$$\frac{1}{n}\frac{d\rho_{xy}}{dB} \times B \cong \alpha\rho_{xx} \tag{6.4}$$

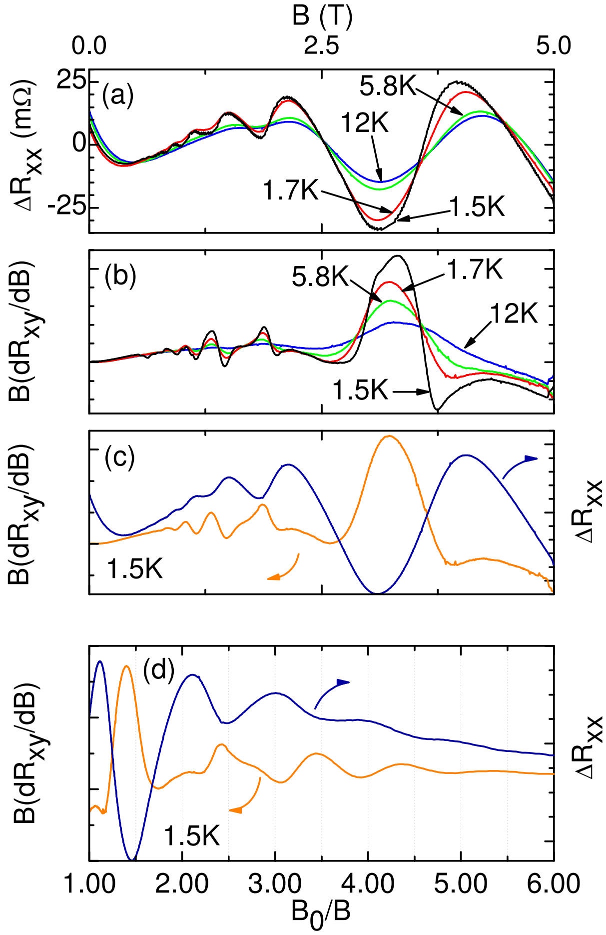

Figure 6.6 Panels (a) and (b) show that the phase of the oscillatory ΔR_{xx} and $B \times dR_{xy}/dB$ does not change with T. (c) Comparison of ΔR_{xx} and $B \times dR_{xy}/dB$ at $T = 1.5$ K. (d) ΔR_{xx} and $B \times dR_{xy}/dB$ are shown vs B_0/B. Both (c) and (d) suggest a phase shift of approximately π between ΔR_{xx} and $B \times dR_{xy}/dB$.

where n is the carrier density, and α is a constant. For a constant n we have,

$$B \times \frac{dR_{xy}}{dB} \propto R_{xx}. \tag{6.5}$$

Now we can apply this empirical relation, eq. (6.5), to the experimental quantities R_{xx}, R_{xy} obtained for thin HOPG specimens.

For the resistivity rule study,[36, 99, 109, 110] the temperature dependences of ΔR_{xx} and $B \times dR_{xy}/dB$ are shown in Figure 6.6 (a) and (b), respectively. Figure 6.6 indicates a progressive change, where the oscillatory amplitude increases with decreasing T while the B-

values of the extrema remains unchanged with T. Figure 6.1 (c) shows the ΔR_{xx} (right axis) and $B \times dR_{xy}/dB$ (left axis) for the sample $S1$ at 1.5 K. A direct comparison [see Figure 6.6 (c)] reveals a π phase difference between $B \times dR_{xy}/dB$ and ΔR_{xx}, i.e, $B \times dR_{xy}/dB \approx -\Delta R_{xx}$. Plots of ΔR_{xx} and $B \times dR_{xy}/dB$ vs B_0/B, [see Figure 6.6 (d)] confirm an approximately π phase shift between ΔR_{xx} and $B \times dR_{xy}/dB$. This variance from the canonical resistivity rule is consistent with the observed type-IV phase relation between the oscillatory R_{xx} and R_{xy} (see Figure 6.5).

6.6 Summary

Low temperature magnetotransport studies carried out on highly oriented pyrolytic graphite indicate strong oscillatory R_{xy} and R_{xx}, with plateaus in Hall resistance R_{xy} with concurrent non-vanishing R_{xx}. Furthermore, a comparative study of the SdH effect and Berry's phase of graphite with those in other systems such bulk $Hg_{0.8}Cd_{0.2}Te$, HgTe quantum well, the 3D n-GaAs epilayer, InSb, the GaAs/AlGaAs 2D electron system, 3D AlGaN, and a graphite intercalation compound, $C_{9.3}AlCl_{3.4}$, reveals a value of $n_0 = 1/2$ in the $B^{-1} \longrightarrow 0$ limit only for the graphene based systems. As in graphene, this feature might reflect a non-zero Berry's phase ($\beta = 1/2$) and Dirac carriers in graphite. In addition, a careful study of oscillatory R_{xy} and R_{xx} reveals an anomalous ("type-IV") phase relation between oscillatory R_{xy} and R_{xx}, and the observed "type-IV" phase relation appear to be consistent over the entire temperature range investigated. The resistivity rule analysis of the transport, however, indicates that $B \times dR_{xy}/dB \approx -\Delta R_{xx}$, and this result is consistent with the observed phase relations between the oscillatory R_{xx} and R_{xy}.

CHAPTER 7

CONCLUSIONS

This work presents an analysis of low temperature magnetotransport in GaAs/AlGaAs heterostructure 2DES and 3D HOPG. Studies on GaAs/AlGaAs heterostructure devices in the presence of microwave photoexcitation mainly focused on investigating possibility of electron heating due to MW radiation and the effect polarization of direction of the linearly polarized microwaves.

The experimental investigation carried out studying the electron heating due to MW radiation indicates that when the 2DES is subjected to adequate microwave radiation, sufficient to induce strong microwave induced resistance oscillations, the effect of the incident radiation on the amplitude of the SdH oscillations over the magnetic field considered is negligible. Consequently, a relatively small increase in the electron temperature is observed, in good agreement with theoretical predictions.

The polarization dependence of the MIMO amplitude represents the first experimental evidence of the sensitivity of MIMO to the polarization direction of the linearly polarized microwaves. Three main features of the polarization dependence study can be identified. First, amplitude of the MIMO at a maximum or a minimum presents a sinusoidal variation with the polarization angle θ at low power, and can be fitted with the function $R_{xx}(\theta) = A \pm C\cos^2(\theta - \theta_0)$, where plus $(+)$ represents a maximum and minus $(-)$ represents a minimum. Second, the variation of phase shift extracted from the NLSFs varies with the physical parameters microwave frequency f, magnetic field B, and sign of the magnetic field. It is important to mention that the value of θ_0 appeared to be independent of the radiation power. Third, at higher radiation power, the principal resistance minimum of MIMO exhibits additional extrema versus the polarization angle.

Magnetotransport studies of highly oriented pyrolitic graphite indicates strong oscillatory R_{xy} and R_{xx}, with Hall (R_{xy}) plateaus coincident with a non-vanishing R_{xx} at the lowest T. Furthermore, a comparative study of SdH Berry's phase of graphite with other systems like the 3D n-GaAs epilayer, the GaAs/AlGaAs 2D electron system, HgTe quantum well, bulk $Hg_{0.8}Cd_{0.2}Te$, 3D AlGaN, InSb, and $C_{9.3}AlCl_{3.4}$ (a graphite intercalation compound) reveals a value of $n_0 = 1/2$ in the $B^{-1} \longrightarrow 0$ limit only for the graphene based systems. As in graphene, this feature might reflect a non-zero Berry's phase ($\beta = 1/2$) and Dirac carriers in graphite. On the other hand, a study of the oscillatory diagonal- and Hall- resistances reveals also an anomalous "type-IV" phase relation between oscillatory R_{xx} and R_{xy}, over the entire temperature range. This result is consistent with the observation of $B \times dR_{xy}/dB \approx -\Delta R_{xx}$ in the resistivity rule analysis of the transport in HOPG specimen.

We hope that the results obtained in this study will contribute to a better understanding of the transport of charge carriers in reduced dimensions upon an applied magnetic field. Specifically the observation of a polarization dependence of the MIMO in GaAs/AlGaAs 2DES heterostructure devices will steer the experimental and theoretical investigations of MIMO in a new direction. Further experimental investigations will be needed to understand the dependence of the phase shift θ_0 on physical parameters such as frequency, magnetic field, etc. Also the "type-IV" phase relation between the Hall- and diagonal- resistances should be investigated more to understand the behaviour of these oscillations.

REFERENCES

[1] A. Y Shik, *Quantum wells : Physics and Electronics of Two-Dimensional Systems* (Wolrd Scientific, River Edge, N.J., 1997).

[2] N. W. Ashcroft, N. D. Mermin, *Solid State Physics* (Brooks/Cole, 1976).

[3] T. Ando, A. Fowler, and F. Stern, Rev. Mod. Phys. 54, 452 (1982).

[4] M. Shayegan, arXiv:cond-mat/0505520v1

[5] K. von Klitzing, G. Dorda, and M. Pepper, Phys. Rev. Lett. 45, 494 (1980).

[6] D. C. Tsui, H. L. Störmer, and A. C. Gossard, Phys. Rev. Lett. 48, 1559 (1982).

[7] R. R. Laughlin, Phys. Rev. Lett. 50, 1395 (1983).

[8] R. Dingle, H. L. Störmer, A. C. Gossard, and W. Wiegmann, Appl. Phys. Lett. 33, 665 (1978).

[9] H. L. Störmer, R. Dingle, A. C. Gossard, W. Wiegmann, and R. A. Logan, *Proc. 14-th Int. Conf. Phys. Semiconductors, Edinburgh, 1978*, ed. B. L. H. Wilson (The Institute of Physics, Bristol, 1978) p. 557.

[10] R. G. Mani, K. von Klitzing, Z. Phys. B 100, 635 (1996).

[11] R. G. Mani, J. H. Smet, K. von Klitzing, V. Narayanamurti, W. B. Johnson, and V. Umansky, Nature (London) 420, 646 (2002).

[12] W. de Lange, F. A. P. Blom, and J. H. Wolter, Semicond. Sci. Technol. 8, 341 (1993).

[13] J. Inarrea, R. G. Mani, and W. Wegscheider, Phys. Rev. B 82, 205321 (2010)

[14] R. E. Prange and S. M. Girvin, *The Quantum Hall Effect*, 2nd. ed. (Springer, New York, 1990).

[15] S. Das Sarma and A. Pinczuk, *Perspectives in Quantum Hall Effects* (Wiley, New York, 1996).

[16] M. A. Zudov, R. R. Du, L. N. Pfeiffer, and K. W. West, Phys. Rev. Lett. 90, 046807 (2003).

[17] S. Dorozhkin, JETP Lett. 77, 577 (2003).

[18] R. G. Mani, V. Narayanamurti, K. von Klitzing, J. H. Smet, W. B. Johnson, and V. Umansky, Phys. Rev. B 69, 161306 (2004); 70, 155310 (2004).

[19] R. G. Mani, J. H. Smet, K. von Klitzing, V. Narayanamurti1, W. B. Johnson, and V. Umansky, Phys. Rev. Lett. 92, 146801 (2004); Phys. Rev. B 69, 193304 (2004).

[20] R. G. Mani, Physica E (Amsterdam) 22, 1 (2004); ibid. 25, 189 (2004).

[21] R. G. Mani, Appl. Phys. Lett. 85, 4962 (2004).

[22] A. E. Kovalev, S. A. Zvyagin, C. R. Bowers, J. L. Reno, and J. A. Simmons, Solid State Commun. 130, 379 (2004).

[23] S. A. Studenikin, M. Potemski, P. T. Coleridge, A. S. Sachrajda, and Z. R. Wasilewski, Solid State Commun. 129, 341 (2004).

[24] R. R. Du, M. A. Zudov, C. L. Yang, L. N. Pfeiffer, and K. W. West, Physica E (Amsterdam) 22, 7 (2004).

[25] I. V. Kukushkin, M. Yu. Akimov, J. H. Smet, S. A. Mikhailov, K. von Klitzing, I. L. Aleiner, and V.I. Falko, Phys. Rev. Lett. 92, 236803 (2004).

[26] R. G. Mani, IEEE Trans. Nanotechnol. 4, 27 (2005); Phys. Rev. B 72, 075327 (2005); Sol. St. Comm. 144, 409 (2007); Appl. Phys. Lett. 92, 102107 (2008); Physica E 40, 1178 (2008).

[27] B. Simovic, C. Ellenberger, K. Ensslin, H.-P. Tranitz, and W. Wegscheider, Phys. Rev. B 71, 233303 (2005).

[28] J. H. Smet, B. Gorshunov, C. Jiang, L. Pfeiffer, K. West, V. Umansky, M. Dressel, R. Meisels, F. Kuchar, and K. von Klitzing, Phys. Rev. Lett. 95, 116804 (2005).

[29] S. I. Dorozhkin, J. H. Smet, V. Umansky, and K. von Klitzing, Phys. Rev. B 71, 201306(R) (2005).

[30] Z. Q. Yuan, C. L. Yang, R. R. Du, L. N. Pfeiffer, and K. W. West, Phys. Rev. B 74, 075313 (2006).

[31] R. G. Mani, Appl. Phys. Lett. 91, 132103 (2007).

[32] S. A. Studenikin, A. S. Sachrajda, J. A. Gupta, Z. R. Wasilewski, O. M. Fedorych, M. Byszewski, D. K. Maude, M. Potemski, M. Hilke, K. W. West and L. N. Pfeiffer, Phys. Rev. B 76, 165321 (2007).

[33] K. Stone, C. L. Yang, Z. Q. Yuan, R. R. Du, L. N. Pfeiffer and K. W. West, Phys. Rev. B 76, 153306 (2007).

[34] A. Wirthmann, B. D. McCombe, D. Heitmann, S. Holland, K.-J. Friedland, and C.-M. Hu, Phys. Rev. B 76, 195315 (2007).

[35] S. Wiedmann, G. M. Gusev, O. E. Raichev, T. E. Lamas, A. K. Bakarov, and J. C. Portal, Phys. Rev. B 78, 121301(R) (2008).

[36] R. G. Mani, W. B. Johnson, V. Umansky, V. Narayanamurti, and K. Ploog, Phys. Rev. B 79, 205320 (2009).

[37] R. G. Mani, C. Gerl, S. Schmult, W. Wegscheider, and V. Umansky, Phys. Rev. B. 81, 125320 (2010).

[38] O. M. Fedorych, M. Potemski, S. A. Studenikin, J. A. Gupta, Z. R. Wasilewski, and I. A. Dmitriev, Phys. Rev. B 81, 201302 (2010).

[39] A. N. Ramanayaka, R. G. Mani, and W. Wegscheider, Phys. Rev. B 83, 165303 (2011).

[40] A. C. Durst, S. Sachdev, N. Read, and S. M. Girvin , Phys. Rev. Lett. 91, 086803 (2003).

[41] A. V. Andreev, I. L. Aleiner, and A. J. Millis, Phys. Rev. Lett. 91, 056803 (2003).

[42] V. Ryzhii and A. Satou, J. Phys. Soc. Jpn. 72, 2718 (2003).

[43] X. L. Lei and S. Y. Liu, Phys. Rev. Lett. 91, 226805 (2003).

[44] P. H. Rivera, P. A. Schulz, Phys. Rev. B 70, 075314 (2004).

[45] X. L. Lei, J. Phys.: Condens. Matter 16, 4045 (2004).

[46] S. A. Mikhailov, Phys. Rev. B 70, 165311 (2004).

[47] J. Inarrea and G. Platero, Phys. Rev. B 72, 193414 (2005).

[48] J. Inarrea and G. Platero, Phys. Rev. B 76, 073311 (2007).

[49] X. L. Lei and S. Y. Liu, Phys. Rev. B 72, 075345 (2005).

[50] I. A. Dmitriev, M. G. Vavilov, I. L. Aleiner, A. D. Mirlin, and D. G. Polyakov, Phys. Rev. B 71, 115316 (2005).

[51] J. Inarrea and G. Platero, Phys. Rev. Lett. 94, 016806 (2005).

[52] A. Auerbach et al., Phys. Rev. Lett. 94, 196801 (2005).

[53] J. Inarrea and G. Platero, Appl. Phys. Lett. 89, 052109 (2006); ibid. 89, 172 114 (2006); ibid. 90, 172118 (2007); ibid. 90, 262101 (2007); ibid. 92, 192113 (2008); Phys. Rev. B 80, 193302 (2009).

[54] J. Inarrea and G. Platero, Phys. Rev. B 78, 193310 (2008).

[55] A. D. Chepelianskii, A. S. Pikovsky, and D. L. Shepelyansky, Eur. Phys. J. B 60, 225 (2007).

[56] A. Auerbach and G. V. Pai, Phys. Rev. B 76, 205318 (2007).

[57] I. A. Dmitriev, A. D. Mirlin, and D. G. Polyakov, Phys. Rev. B 75, 245320 (2007).

[58] P. H. Rivera, A. L. C. Pereira, and P. A. Schulz, Phys. Rev. B 79, 205406 (2009).

[59] I. G. Finkler and B. I. Halperin, Phys. Rev. B 79, 085315 (2009).

[60] X. L. Lei and S. Y. Liu, Appl. Phys. Lett. 94, 232107 (2009).

[61] A. D. Chepelianskii and D. L. Shepelyansky, Phys. Rev. B 80, 241308(R) (2009).

[62] D. Hagenmüller, S. De Liberato, and C. Ciuti, Phys. Rev. B 81, 235303 (2010).

[63] M. Tinkham, *Introduction of Superconductivity*, 2nd. ed. (McGraw-Hall, New York, 1996).

[64] R. G. Mani, J. H. Smet, K. von Klitzing, V. Narayanamurti, W. B. Johnson, and V. Umansky, Phys. Rev. Lett. 92, 146801 (2004); Phys. Rev. B 69, 193304 (2004); ibid. 69, 161306 (2004); ibid. 70, 155310 (2004).

[65] R. G. Mani, J. H. Smet, K. von Klitzing, V. Narayanamurti, and V. Umansky, Bull. Am. Phys. Soc. 46, p. 972 (2001);
http://flux.aps.org/meetings/YR01/MAR01/abs/S7750003.htm6.

[66] M. A. Zudov, R. R. Du, J. A. Simmons, and J. L. Reno, Phys. Rev. B 64, 201311 (2001).

[67] P. D. Ye, L. W. Engel, D. C. Tsui, J. A. Simmons, J. R. Wendt, G. A. Vawter, and J. L. Reno, Appl. Phys. Lett. 79, 2193 (2001).

[68] R. G. Mani, J. H. Smet, K. von Klitzing, V. Narayanamurti, W. B. Johnson, and V. Umansky, in the Proc. 26th Intl. Conf. Phys. of Semicond., Edinnburgh, Scotland, 29 July - 2 Aug. 2002, IOP Conf. Series 171, eds. A. C. Long and J. H. Davies (IOP, Bristol, 2003) H112.

[69] D. Konstantinov and K. Kono, Phys. Rev. Lett. 103, 266808 (2009); Phys. Rev. Lett. 105, 226801 (2010).

[70] R. G. Mani, A. N. Ramanayaka, and W. Wegscheider, Phys. Rev. B 84, 085308 (2011).

[71] A. N. Ramanayaka, R. G. Mani, J. Inarrea, and W. Wegscheider, Phys. Rev. B 85, 205315 (2012).

[72] V. Ryzhii and R. Suris, J. Phys.: Cond. Matt. 15, 6855 (2003).

[73] A. A. Koulakov and M. E. Raikh, Phys. Rev. B 68, 115324 (2003).

[74] S. Y. Liu, and X. L. Lei, J. Phys.: Condens. Matter 15, 4411 (2003).

[75] I. A. Dmitriev, A. D. Mirlin, and D. G. Polyakov, Phys. Rev. Lett. 91, 226802 (2003).

[76] J. Inarrea and G. Platero, J. Phys. Conf. Ser. 210, 012042 (2010).

[77] I. A. Dmitriev, M. Khodas, A. D. Mirlin, D. G. Polyakov, and M. G. Vavilov, Phys. Rev. B 80, 165327 (2009).

[78] S. A. Mikhailov, Phys. Rev. B 83, 155303 (2011); ibid. 71, 035320 (2005).

[79] N. H. Lindner, G. Refael, and V. Galitski, Nat. Phys. 7, 490 (2011).

[80] Z. Gu, H. A. Fertig, D. P. Arovas, and A. Auerbach, arXiv:1106.0302v1.

[81] C. Nayak, S. H. Simon, A. Stern, M. Freedman, S. Das Sarma, Rev. Mod. Phys. 80, 1083 (2008).

[82] I. Zutic, J. Fabian, and S. Das Sarma, Rev. Mod. Phys 76, 323 (2004).

[83] Y. Zheng and T. Ando, Phys. Rev. B 65, 245420 (2002).

[84] K. S. Novoselov et al. Science 306, 666 (2004).

[85] C. Berger, Z. Song, T. Li, X. Li, A. Y. Ogbazghi, R. Feng, Z. Dai, A. N. Marchenkov, E. H. Conrad, P. N. First, and W. A. de Heer, J. Phys.Chem. B 108, 19912 (2004).

[86] A. K. Geim and K. S. Novoselov, Nat. Matl. 6, 183 (2007).

[87] M. V. Berry, Proc. R. Soc. London A 392, 45 (1984).

[88] G. P. Mikitik and Y. V. Sharlai, Phys. Rev. Lett. 82, 2147 (1999).

[89] Y. Zhang, Y. Tan, H. L. Stormer and P. Kim, Nature 438, 10 (2005).

[90] J. W. McClure, Phys. Rev. 108, 612 (1957).

[91] D. E. Soule, J. W. McClure, and L. B. Smith, Phys. Rev. 134, A453 (1964); J. R. Anderson, W. J. O'Sullivan, J. E. Schirber, and D. E. Soule, Phys. Rev. 164, 1038 (1967).

[92] S. J. Williamson, S. Foner, and M. S. Dresselhaus, Phys. Rev. 140, A1429 (1965).

[93] I. A. Luk'yanchuk and Y. Kopelevich, Phys. Rev. Lett. 93, 166402 (2004).

[94] H. Kempa, P. Esquinazi, and Y. Kopelevich, Sol. St. Comm. 138, 118 (2006).

[95] I. A. Luk'yanchuk and Y. Kopelevich, Phys. Rev. Lett. 97, 256801 (2006). See also: J. M. Schneider, M. Orlita, M. Potemski, and D. K. Maude, Phys. Rev. Lett. 102, 166403 (2009).

[96] S. Y. Zhou, G. -H. Gweon, J. Graf, A. V. Fedorov, C. D. Spataru, R. D. Diehl, Y. Kopelevich, D. -H. Lee, S. G. Louie, and A. Lanzara, Nat. Phys. 2, 595 (2006).

[97] H. L. Stormer, J. P. Eisenstein, A. C. Gossard, W. Wiegmann, and K. Baldwin, Phys. Rev. Lett. 56, 85 (1985).

[98] B. A. Bernevig, T. L. Hughes, S. Raghu, and D. P. Arovas, Phys. Rev. Lett. 99, 146804 (2007).

[99] A. M. Chang and D. C. Tsui, Sol. St. Comm., 56, 153 (1985).

[100] Y. Kopelevich, J. H. S. Torres, R. R. da Silva, F. Mrowka, H. Kempa, and P. Esquinazi, Phys. Rev. Lett. 90, 156402 (2003).

[101] R. G. Mani, J. Phys. Soc. Jpn. 65, 1751 (1996).

[102] R. G. Mani, Phys. Rev. B 41, 7922 (1990).

[103] X. C. Zhang, A. Pfeuffer-Jeschke, K. Ortner, C. R. Becker, and G. Landwehr, Phys. Rev. B 65, 045324 (2002).

[104] D. Jena, S. Heikman, J. S. Speck, A. Gossard, U. K. Mishra, A. Link, and O. Ambacher, Phys. Rev. B 67, 153306 (2003).

[105] G. Nachtwei, N. J. Bassom, W. Kraak, R. J. Nicholast, and M. Watts, Semicond. Sci. Technol. 8, S168-Sl71 (1993).

[106] V. A. Kulbachinskii, S. G. Ionov, S. A. Lapin, and A. de Visser, Phys. Rev. B 51, 10313 (1995).

[107] M. Orlita, C. Faugeras, G. Martinez, D. K. Maude, M. L. Sadowski, J. M. Schneider, and M. Potemski, J. Phys.: Cond. Matter 20, 454223 (2008).

[108] W. Pan, J. S. Xia, H. L. Stormer, D. C. Tsui, C. L. Vicente, E. D. Adams, N. S. Sullivan, L. N. Pfeiffer, K.W. Baldwin, and K.W. West, Phys. Rev. Lett. 95, 066808 (2005).

[109] T. Rötger, G. J. C. L. Bruls, J. C. Maan, P. Wyder, K. Ploog, and G. Wiemann, Phys. Rev. Lett. 62, 90 (1989).

[110] H. P. Wei, D. C. Tsui, M. A. Paalanen, and A. M. M. Pruisken, Phys. Rev. Lett. 61, 1294 (1988).

[111] A. N. Ramanayaka, R. G. Mani, Phys. Rev. B 82, 165327 (2010).

[112] Convertion of 4He vapour presure to temperature was done by using the applet available at the following website: http://www.qdusa.com/techsupport/hvpCalculator.html

Appendix A

EXPERIMENTAL APPARATUS

Measurements reported here have been carried out in an Oxford instruments liquid ^{4}He cryostat with a superconducting solenoid magnet, which is capable of providing a maximum magnetic field of 14 T at 4.2 K. The temperature can be varied using the variable temperature inset (VTI) from 400 K to 1.5 K, and the procedure used to control the temperature is discussed in Appendix A.2.

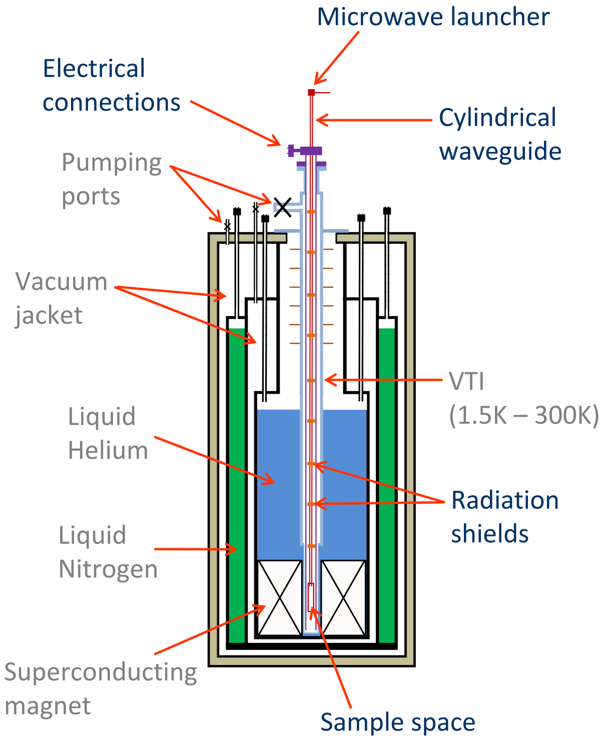

Figure A.1 Schematic of the liquid ^4He cryostat and the sample holder is shown. The text in the light color shows the parts of the cryostat and the dark text shows the parts of the sample holder.

A specially designed sample probe, see Appendix A.1, was used to load the specimens into the cryostat and carry out the experiment at temperatures as low as 1.5 K at dark (w/o MW) as well as in the presence of continuous microwave radiation. A schematic of the experimental setup is shown in Figure A.1, where the lighter text represents the parts that belong to the cryostat and the dark text shows the parts that belong to the sample probe.

Microwave radiation was generated using an Agilent 83650B synthesized swept-signal generator, 0.01-50 GHz. Frequencies above 50 GHz, 60-120 GHz, were generated using a mm-wave source module from OML, inc., driven by the Agilent 83650B synthesizer.

A.1 Sample probe

The sample probe used in the experiments reported here was specially designed to have properties such as:

- Ability change the polarization direction of linearly polarized microwaves with respect to the specimen.
- Ability to use with different types of chip carriers without any changes to its original wiring.
- Availability of large number (≈ 25) of electrical connections providing the opportunity to measure several signals or several samples at a given time.
- Low thermal conduction into the sample space enabling the capability of reaching low temperatures.

As mentioned earlier, approximately 6 foot long cylindrical waveguide (11 mm i.d.) was used to deliver microwaves to the specimen and the sample probe was designed such that rest of the parts fit on the waveguide (see Figure A.2). Outer stainless steel tube, $1''$ o.d., provides protection for the wires and also acts as a vacuum chamber covering the upper part of the probe. Lower cut-off frequency for the cylindrical waveguide is about 16 GHz; therefore, two semi-rigid coaxial waveguides were also included in the probe in order to access the lower frequencies.

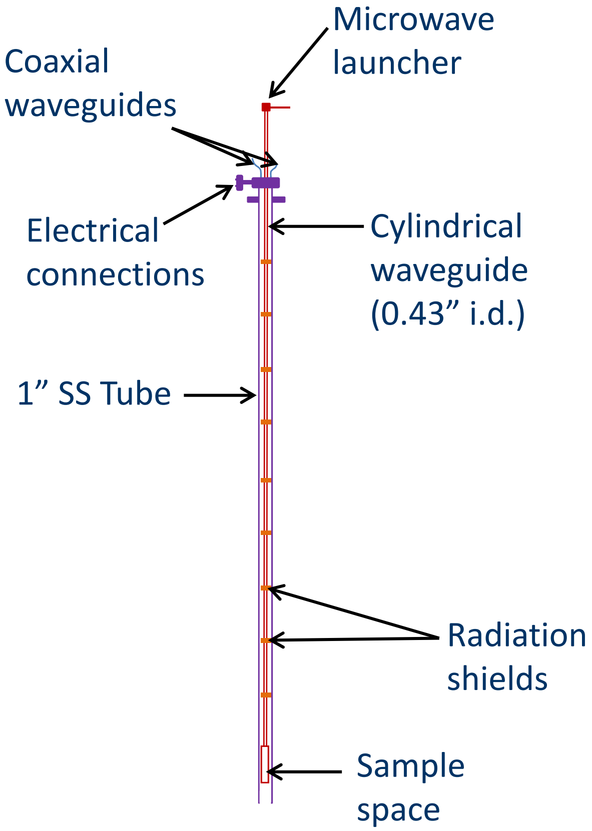

Figure A.2 Schematic of the sample probe.

Radiation shields have been used to reduce the heat load coming into the sample space, and the same shields have been used to heat sink all the wires going into the system. In the current design, there are 25 connections available for measuring electrical signals from the specimen. Apart from these connections, there are 18 other connections available for thermometers, heater, LED, etc. The upper part of the probe is carefully designed such that there are no air leaks into the sample space.

The bottom part of the sample probe was designed to accommodate different sample mounts described in Appendix A.1.2. Also the design of the end part of the sample holder only allows the sample mounts to be attached in one orientation providing the same relative orientation of the MW-antenna and the sample mount.

A.1.1 Setting the MW polarization direction

The MW launcher was designed to generate linearly polarized TE modes in the waveguide. Proper design of the launcher and the choice of a cylindrical waveguide allows us to change the polarization direction of the linearly polarized microwaves relative to a fixed direction. It is important, however, to make sure that this scheme works as expected; therefore, we carried out a simple experiment, at room temperature, by placing a MW detector, which is sensitive to the polarization direction of linearly polarized microwaves, at the sample end of the probe. The detector orientation was fixed at a desired orientation and then the MW launcher was rotated 360°. Results of this experiment are shown in Figure A.3.

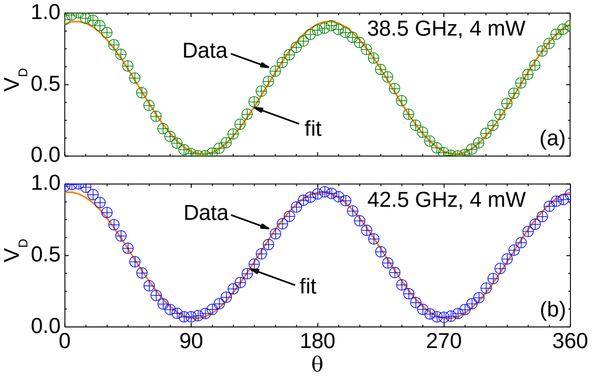

Figure A.3 Normalized detector response vs the polarization angle is shown for (a) 38.5 GHz and (b) 42.5 GHz. Here the circles represent the data and the solid line represents the NLSF fit.

Here the polarization angle was defined as the angle between the antenna in the MW launcher and the antenna in the MW detector. A sinusoidal variation of the MW detector response to the polarization angle (see Figure A.3) confirms that the MW polarization is preserved until the end of the sample probe. In addition, a NLSF fit to a cosine squared function,

$$V_D = A + B\cos^2(\theta + \theta_0) \tag{A.1}$$

would allows us to obtain a phase shift, θ_0, associated with the measurement at a given frequency, and this phase shift can be considered as the experimental uncertainty of measuring the polarization angle. Phase shifts obtained for a range of microwave frequencies [see Figure 5.2 (b)] indicate that the uncertainty associated with θ is about ±10°.

A.1.2 Sample mount

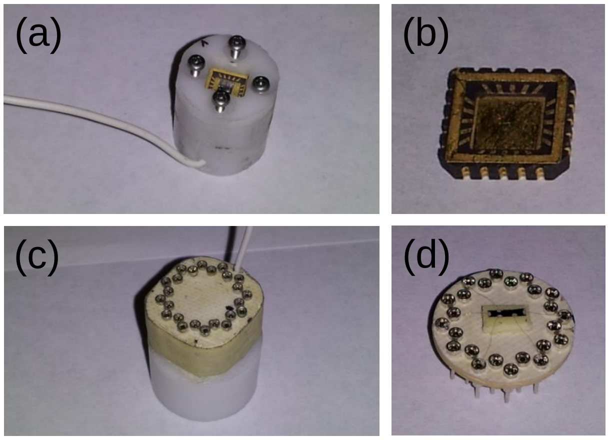

Figure A.4 Sample mounts used with (a) 20 pin LLCC sample carriers shown in (b), and (c) 24 pin circular sample carriers shown in (d).

Before the measurements, the devices (or samples) have to be connected to the sample probe, and this connection was done by using a specially designed sample mount. Two type of sample carriers have been used during the experiments. Typically the GaAs/AlGaAs heterostructure devices were mounted on a 20 pin LLCC (leadless chip carrier) [see Figure A.4 (b)] and HOPG devices were mounted on a 24 pin circular sample carriers [see Figure A.4 (d)]. Because of the two types of sample carriers used, there were two sample mounts designed to mount the devices to the sample probe [see fig. A.4 (a) and (c)].

A.2 Measuring and controlling the temperature

Accurate measurement of the temperature at the sample and maintaining it at a constant level is important during the measurement. The sample probe was equipped with a silicon diode, and a pair of Allen Bradley resistors (ABR) for temperature measurements. Also there was a Cernox resistor, calibrated by Lake Shore Cryotronics, in the VTI available

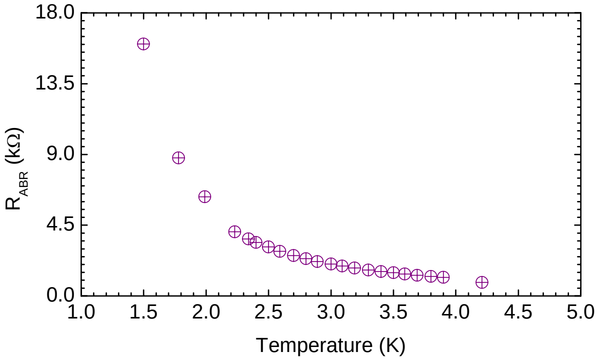

Figure A.5 ABR resistance vs temperature is shown for 75 Ω ABR. Current through the resistor is 0.5 μA.

for temperature measurements as well. The silicon diode was used to measure temperatures above 8 K by using a Lake Shore DRC 93 temperature controller. For temperatures below 5 K, 75 Ω ABR resistors and the silicon diode were calibrated using vapour-pressure thermometry.[112] A calibration curve for 75 Ω ABR is shown in Figure A.5 for temperatures from 4 K to 1.5 K.

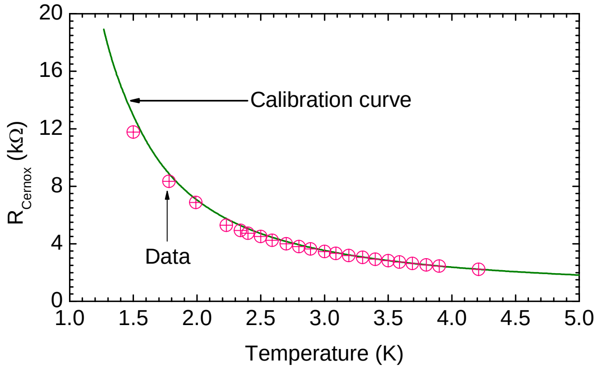

Figure A.6 Cernox resistance vs. temperature is shown. Solid line and the open circles shows the calibration curve and measured values while calibrating ABR, respectively.

During the ABR calibration, the resistance of the Cernox resistor was also recorded. Figure A.6 shows the calibrated values for the Cernox resistor (solid line) as well as the measured resistances (open circles), and both of them are in good agreement.

The sample probe also contains a 25 Ω heater coil for controlling the temperature. The heater was driven by a Lake Shore temperature controller, model DRC-93A, and this method was employed for the temperatures above 8 K only. Beside the heater coil in the sample probe, there is another heater available in the VTI and that also can be used to control the temperature. At low temperatures, $T \leq 4.2$ K, ^{4}He vapour pressure can be used to set the temperature.

Appendix B

ELECTRICAL MEASUREMENTS

In a typical experiment, low frequency lock-in techniques have been used to measure the electrical signals from the specimen. As shown in Figure B.1, there is a low frequency ($f_{current} \leq 15$ Hz) AC current passing through the specimen and phase locked amplifiers working at the same frequency, $f_{current}$, are used to detect the electrical signals (V_{xx} or V_H) from the specimen.

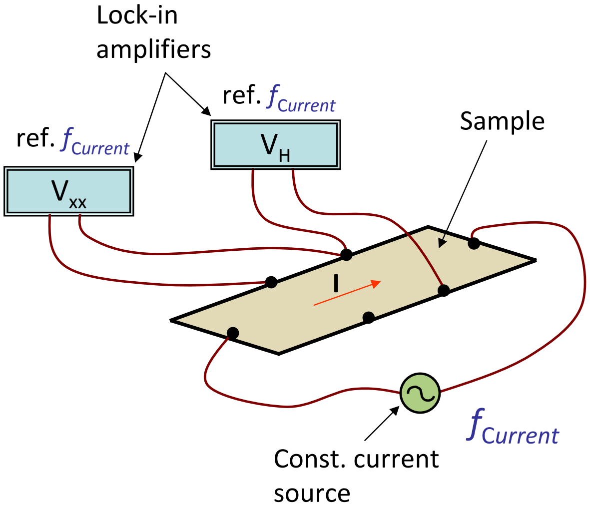

Figure B.1 Schematic of the electrical connections for a typical measurement is shown. A constant current source sends a low frequency, $f_{current}$, AC current though the specimen, and the same frequency is used as the reference of the lock-in amplifiers, which measure the voltages across given two contacts.

Instead of a constant current source, one can use a constant voltage source with a large resistor in series with the specimen and still achieve the constant current condition (see Figure B.2). The oscillator output of a lock-in amplifier can be used as the constant voltage source, and the TTL output of the same lock-in can be used as the reference signal for the other lock-in amplifiers. In the following section, Appendix B.1, I characterize the constant current source that has been used in the experiments, and I assures the stability of the current under typical experimental conditions.

B.1 Constant current supply

A schematic of an equivalent circuit for a constant current source is shown in Figure B.2. By applying Kirchhoff's voltage low to this circuit, one can find the current through the circuit as

$$\begin{aligned} I(t) &= \frac{V(t)}{R_L + R_S} \\ &= \frac{V(t)}{R_L}\left(1 + \frac{R_S}{R_L}\right)^{-1} \\ &= \frac{V(t)}{R_L}\left[1 - \left(\frac{R_S}{R_L}\right) + \left(\frac{R_S}{R_L}\right)^2 - \left(\frac{R_S}{R_L}\right)^3 + \ldots\right]. \end{aligned} \tag{B.1}$$

Under typical experimental conditions the sample resistance at zero magnetic field is about 4Ω, i.e., $R_S \approx 4\ \Omega$ and $R_L \approx 10^6\ \Omega$; therefore, for $R_S << R_L$, the current through the circuit is

$$I_0(t) \simeq \frac{V(t)}{R_L} \tag{B.2}$$

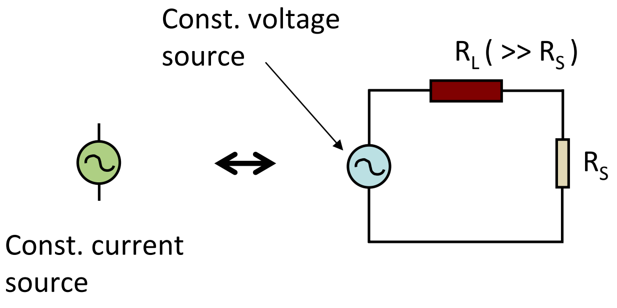

Figure B.2 Schematic of a electrically equivalent circuit of a constant current source using a constant voltage source. Here R_S is the load (sample) resistance and R_L is the current limiting resistor, where $R_L >> R_S$.

which is independent of the sample resistance, R_S. Now let us suppose the sample resistance, R_S, increases by a factor of 100, which is highly unlikely under the experimental conditions reported in here. In such a situation one can calculate the first order correction ($|\Delta I(t)|$), as the higher orders will be negligible for $R_S/R_L << 1$.

$$\begin{aligned} I(t) &= \frac{V(t)}{R_L}\left[1 - \left(\frac{100 \times R_S}{R_L}\right)\right] \\ &= I_0(t) - \frac{V(t)}{R_L}\left(\frac{100 \times R_S}{R_L}\right) \\ |\Delta I(t)| &= 100\left(\frac{R_S}{R_L}\right) I_0(t) \end{aligned} \tag{B.3}$$

Now for the typical values of R_L and R_S, the value of $|\Delta I(t)|$ is

$$|\Delta I(t)| = 0.0004 \times I_0(t) \tag{B.4}$$

about 0.0004 times smaller than $I_0(t)$. Consequently, the current source shown in Figure B.2 provide a constant current with an accuracy of 99.96% under the typical experimental conditions.

B.2 Low noise electrical measurements

Phase sensitive detection of electrical signals is an extremely powerful technique for detecting very small electrical signals in a noisy environment. Use of lock-in amplifiers for phase sensitive detection of electrical signals is a well known method for achieving higher signal to noise ratios in the measured signal.

Typically, the experiment is executed at a known frequency, and the same frequency is used as the reference of the lock-in amplifiers that are been used to detect the signals. Let us assume for simplicity that the reference signal is of the form of

$$V_{ref} = V_r \sin(\omega_r t + \phi_r) \tag{B.5}$$

where V_r, ω_r, and ϕ_r are the amplitude, frequency and the phase of the reference signal. Also let us assume the signal to be measured also has a similar form

$$V_{sig} = V_s \sin(\omega_s t + \phi_s) \tag{B.6}$$

where V_s, ω_s, and ϕ_s are the amplitude, frequency and the phase of the signal to be measured. Then the lock-in amplifier amplifies the signal from the experiment and then multiplies the amplified signal with the reference signal using a phase sensitive detector. Let us take the output of the phase sensitive detector as V_{PSD},

$$V_{PSD} = \frac{1}{2} V_s V_r (\cos[(\omega_s - \omega_r)t + (\phi_s - \phi_r)] - \cos[(\omega_s + \omega_r)t + (\phi_s + \phi_r)]) \tag{B.7}$$

Under normal experimental conditions $\omega_r = \omega_s$ $(= \omega_0)$, hence from eq. (B.7),

$$V_{PSD} = \frac{1}{2} V_s V_r \cos(\phi_s - \phi_r) - \frac{1}{2} V_s V_r \cos(2\omega_0 t + \phi_s + \phi_r). \tag{B.8}$$

Finally the output of the phase sensitive detector will pass through a low pass filter to remove the higher frequencies and harmonics of the reference frequency in eq. (B.8). At this point the output of the lock-in amplifier provides a measure of the signal from the experiment, and one can tune the phase of the reference signal ϕ_r in order to maximize the in-phase measured signal.

Appendix C

SAMPLE PREPARATION

C.1 GaAs/AlGaAs Hall bar devices

Measurements on 2DES were performed on high quality MBE grown GaAs/AlGaAs heterostructure material provided by Dr. Werner Wegscheider's group at ETH Zürich. Standard Hall bar geometry devices were patterned on the GaAs/AlGaAs wafer using optical lithography followed by chemical etching. In order to deposit metal contacts, the devices were masked using photoresist by optical lithography, followed by deposition of a layer of Gold-Germanium (AuGe) and Nickel (Ni) in a UHV electron-beam evaporater, lifftoff, and alloying in a vacuum furnace. Then another layer of Au and Chromium (Cr) were deposited on top of AuGe/Ni contacts. Then the devices were separated, mounted on 20 pin LLCCs [see Figure A.4 (b)] and wire bonded to the chip carrier.

C.2 HOPG devices

Thin HOPG specimens were exfoliated from bulk HOPG. Exfoliation involves repeated pealing of bulk HOPG until a desired thickness achieved. The HOPG specimens studied here were about 25 μm thick and about 5×3 mm^2 in size. The specimens were mounted on a 24 pin circular sample carrier [see Figure A.4 (d)]. Then electrical connections were made from the specimen to the pins of the sample carrier with gold (Au) wires (size 0.001") using SPI conductive silver paint. Initially 42 AWG copper (Cu) wires were used to make electrical connections from the HOPG specimen to the sample carrier, but the wire was too stiff and the contacts came off of the specimen during the cool down.